Politecnico di Torino
Université Paris-Sud

International Master Course in Physics of Complex Systems

Master Thesis

Pairing and topological phases in cold atoms with long-range interactions

Thesis advisor:

Prof. Fabrizio Dolcini
Politecnico di Torino

Scientific supervisors:

Prof. Guillaume ROUX
Université Paris-Sud

Prof. Leonardo MAZZA
Université Paris-Sud

Prof. Pascal SIMON
Université Paris-Sud

Candidate:

Lorenzo GOTTA
Politecnico di Torino
Matr. 253358

Université Paris-Sud

ACADEMIC YEAR 2018-2019

Contents

Chapter 1

Introduction

The systematic study and classification of phase transitions has become a popular research area in physics over the past decades (see, e.g., [24]). The most familiar phenomena associated to the concept of phase transition are the ones giving rise to macroscopic changes in the properties of strongly correlated many-body systems due to thermal fluctuations. Prominent examples of this kind of behaviour are the ferromagnetic-paramagnetic transition in lattice spin models and the liquid-gas transition.

On the other hand, when dealing with quantum-mechanical systems, matter can change from one state to another as the result of the variation of parameters other than temperature. In particular, as extensively explained in [23], when a given many-body quantum problem is studied at zero temperature, thereby suppressing thermal fluctuations, it is the interplay between kinetic energy and interactions that can cause the system to be into different phases as the model parameters are varied, contrarily to what occurs in classical systems, whose zero-temperature behaviour can be characterized as a fluctuationless ground state configuration. Phase transitions occurring at zero temperature are widely known as quantum phase transitions.

In the framework of the physics of phase transitions, the role of dimensionality is a noticeable one. The major challenge in this perspective is the treatment of low dimensional systems, where standard mean-field treatments and ordinary perturbation theory are known to fail due to the enhancement of quantum fluctuations. The need for a description of collective behaviours in reduced dimensionality is unavoidable in one-dimensional (1D) systems (see [1]), which turn out to be simple enough to be studied in an effective way through both numerical and analytical techniques, while exhibiting a rich and deeply fascinating phenomenology.

Intuitively, since particles confined to one dimension cannot avoid interactions among each other, the typical low energy excitations of the system are represented by collective density waves, which substitute the nearly free quasiparticle excitations characterizing the behaviour of three-dimensional Fermi liquids in the description of the effects of the interplay between kinetic fluctuations

and interactions.

On the other hand, the tools employed in the activity of tackling 1D many-body problems are efficient and well developed. The analytical approaches are mainly based on the bosonization technique ([12], [15], [13]), which allows for the reformulation of strongly correlated 1D systems onto free bosonic theories, which can then be analyzed by means of standard path integral techniques. Meanwhile, the density matrix renormalization group (DMRG) algorithm represents the state-of-the-art numerical machinery in the study of 1D physics ([6], [7]), since it allows to efficiently extract the low energy properties of the model Hamiltonian and consequently characterize the corresponding phase diagram by means of the behaviour of properly chosen order parameters.

As a final remark pointing out the relevance of the research effort in the direction of a better understanding of 1D many-body quantum systems, it is worth noticing that 1D systems do not represent only a playground for theorists, but have been experimentally realized by means of, e.g., setups with ions and cold atoms trapped in optical lattices ([9], [11], [8], [10], [26]), where the experimentalist is able to tune the model parameters by varying the characteristic features of the trapping laser beams and meanwhile has a comfortable access to the most relevant observables. The mission on experimental side consists therefore in the implementation of quantum simulation, i.e. the ability to transcribe the dynamics of an arbitrary many-body Hamiltonian into an engineered cold-atoms platform in such a way that it can be reproduced and easily studied by means of the high degree of control exerted by the experimentalist on the system.

A further platform where the effects of quasi-1D confinement of electrons can be experimentally investigated is represented by the so called nanowires, as briefly discussed in [13]. Those can be defined as metallic or semiconducting structures with a length to width ratio typically of the order of or larger than 10^3 and where the electrons are effectively confined in a cylindric-like region whose transverse diameter has a value of the order of a nanometer, whereas the length of the system can range from hundreds of nanometers to over a hundred of micrometers. At the nanometric scale associated to the transverse confinement quantum effects become overwhelmingly important and the resulting phenomenology gives insights into the nature of collective phenomena in quasi-1D regimes, whose peculiarity is witnessed by, e.g., the realization of conductance quantization in the framework of the nanowire transport properties (see, e.g., [25]).

After having briefly discussed why 1D physics has raised such a huge amount of interest among physicists around the world, let us discuss the concrete goals of the present work. It is widely known that a great part of the short-range interacting systems falls into the Tomonaga-Luttinger liquid universality class, for it is characterized by means of a universal quadratic bosonic massless field theory dependent on two phenomenological parameters which are functions of the microscopic model. The main features of the aforesaid phase are the gapless density wave excitations and the quasi-long-range order, defined by the power

law decay of the correlators. Hence, short-range interactions in one dimension are pretty well understood in their generality, even though, of course, the Luttinger liquid picture is still too restrictive to capture their whole phenomenology: as an example of the possible complications one can face, it is worth reminding us of the Berezinskii-Kosterlitz-Thouless (BKT) transition from the Luttinger liquid phase to a Mott insulating regime exhibited by the XXZ model (see [27]), which we are going to recharacterize during the work thesis.

On the other hand, when one adds interaction terms going beyond the standard on-site and nearest-neighbour contributions to the Hamiltonian of the system under analysis, the resulting phenomenology gets way much richer and has not been fully characterized by the scientific community yet. However, there exist hints that the Tomonaga-Luttinger liquid paradigm is not as ubiquitously valid in such a setting. For example, Dalmonte et al. have argued in [5] that a system of hard-core bosonic particles away from half-filling interacting through a long-range soft-shoulder potential exhibit a transition from a Luttinger liquid phase to a cluster Luttinger liquid one triggered by the increase in the interaction strength. The main point of the characterization of such an exotic quantum liquid phase is the observation that the fundamental granularity of the system is represented by mesoscopic ensembles of particles instead of individual ones, as it is the case for standard Luttinger liquids.

The model Hamiltonian considered by the authors reads:

$$H = -t \sum_j \left[b_j^\dagger b_{j+1} + h.c. \right] + V \sum_j \sum_{l=1}^{r_c} n_j n_{j+l} \tag{1.1}$$

where $b_j, b_j^\dagger$ are bosonic creation and annihilation operators, $n_j = b_j^\dagger b_j$ and t is the tunneling rate. The shape of the interaction potential, assumed to exhibit a soft-core profile with depth V and radius r_c, is an approximation to the effective interaction potential between two atoms in Rydberg-dressed cold gases, where, in the case of a weak dressing regime, the atomic systems in their ground states are off-resonantly coupled to a high-lying Rydberg state by means of a laser field. In such an experimental setting, the aforesaid effective interaction potential has the following expression as a function of the relative distance x:

$$V(x) = \frac{\Omega^4}{8\Delta^3} \frac{r_c^6}{r_c^6 + x^6} \tag{1.2}$$

where the parameters Ω, Δ and the characteristic radius r_c depend, broadly speaking, on the laser field frequency as well as on the atomic system spectrum and on the properties of the addressed Rydberg level with respect to the van der Waals interaction. Hence, while for $x \gg r_c$ one recovers the usual repulsive van der Waals interaction between Rydberg atoms $\propto x^{-6}$, in the regime $x < r_c$ the interaction potential saturates to a constant value as a result of the dipole blockade mechanism, thereby justifying the form of the interaction term introduced in (1.2).

Meanwhile, the experimental machinery required for the purpose of the quantum simulation of systems equipped with long-range interactions has been the

focus of most of the recent research on experimental cold-atoms physics. One of the first milestone works in this direction is [26], whose key idea is the intuition that the pathway to the realization of long-range interactions in ultracold atomic gases relies heavily on the properties exhibited by the Rydberg atoms, as the van der Waals forces between them are many orders of magnitude larger than for the corresponding ground state atoms. Hence, the authors exploited the mere laser excitation of a two-dimensional gas of alkali atoms prepared in a Mott insulating configuration to couple the atomic ground and Rydberg states with the goal of measuring the resulting strong correlations and spatial excitation patterns.

As witnessed by works such as [8], the opportunity of employing Rydberg atoms for quantum simulation purposes has pushed forward the research efforts towards the optimal way to exploit their unique properties. E.g., the aforesaid paper formulates the proposal that the best-suited physical units to be used in the quantum simulation of long-range interacting systems are the so called circular Rydberg atoms, i.e., atoms in a Rydberg state with maximum angular momentum whose distinctive feature is an intrinsically longer lifetime of the corresponding Rydberg state with respect to non-circular states. The latter feature depends crucially on the fact that the main decay channel of the circular level is spontaneous emission on the microwave transition towards the next lower circular level.
The present work is ideally divided into four parts. The first one deals with the definition of the problem with reference to some of the most relevant scientific publications on the topics discussed in the remainder of the thesis report. The included experimental contributions ([8], [9], [26], [11], [28]) involve the definition and main features of a quantum simulator, whereas the theoretical works ([2],[4]) dwell into the exploration of the zero-temperature phase diagram of lattice models containing interaction potentials extending beyond nearest-neighbour sites.

In the second chapter, the bosonization method is developed in great detail by introducing the crucial idea at its foundation and, subsequently, establishing the main formal results employed in the rest of the work while applying the method to the study of 1D lattice models. The bosonization prescription is then applied to the characterization of the spin-$\frac{1}{2}$ XXZ model, so that a firm theoretical foundation to the transition from a Luttinger liquid phase to a long-range antiferromagnetic order the model exhibits can be established. Meanwhile, the analytical results are complemented by numerical evidences of the aforesaid phases obtained by means of original DMRG simulations.

Afterwards, in the third portion of the work we are going to recharacterize the phase diagram of the model discussed in [2] by performing DMRG simulations in all phases exhibited by the model as a function of the parameters contained in the Hamiltonian parameters. In such a setting, we will be looking at the behaviour of the most noticeable ground state observables, such as correlators, density profiles and local kinetic energy plots, in order to phenomenologically detect the different kinds of collective behaviours emerging from the numerical data. These results will then be complemented by the acquisition of

the finite-size scaling of more fundamental order parameters such as the gap in the single-particle excitation spectrum and the bond-order parameter, which will be discussed in more detail while presenting the related numerical results.

The fourth step of the analysis is then directed towards a first introductory understanding of the features of the phase diagram of the very same theoretical model at a lower density with respect to the half-filled case. The reasons for such a choice are deeply rooted in a pioneering idea brought about by Ruhman et al. in [3]. The authors of the work demonstrated in the case of a spinless fermion model with both single-particle and pair hopping the appearence of quasi-degeneracies in the low energy spectrum associated to the emergence of Majorana-like zero-energy modes at the interfaces between a weak pairing liquid phase and a strong pairing one.

Hence, armed with perfectly analogous goals in mind, the ambition of an ideal subsequent development of the project relies on the expectation that it is possible to stabilize a liquid phase of strongly bound pairs by decreasing the density of the overall system in the framework of the model whose properties are going to be the main focus of our investigation. Such an intuition depends crucially on the hope that the aforementioned exotic liquid phase with strong superconducting fluctuations may derive either from a charge-ordered precursor phase whose unit cell is represented as $(\bullet\bullet\circ\circ)$, where the black dots indicate occupied sited and the white dots refer to empty ones, or could be realized by switching on attractive nearest-neighbour interactions. We hope the consequences of more accurate simulations and deeper analytical calculations in this direction could lead to original and fascinating consequences in the world of topological condensed matter physics.

Chapter 2

One-dimensional systems with long-range interactions

2.1 Quantum simulation

The study of quantum many-body physics has always posed serious challenges to theoretical physicists since its birth. Indeed, on one side the analytical approaches and exactly solvable models, despite being relevant to the understanding of the processes undelying the phenomenology of various observed collective effects, are strongly limited to the investigation of few relevant scenarios, whereas on the other the huge number of degrees of freedom and the resulting exponentially large Hilbert space dimension make brute-force exact diagonalization methods on classical computers unapplicable to most interesting setups in condensed matter physics. The density matrix renormalization group (DMRG) algorithm, despite having proven to be extremely successful in the study of one-dimensional physics, still exhibits efficiency performances which depend strongly on the entanglement properties of the system and make it practically useless when dealing with higher-dimensional quantum many-body dynamics.

The ideal tool envisioned from experimental side in order to overcome the aforesaid limitations take the name of quantum simulator and was first proposed by R. P. Feynman (see [29]) in 1982. The key idea of the aforesaid device consists in the proper engineering of a technological instrument which actively exploits quantum mechanics to solve quantum mechanical problems. As far as the computational power of such an approach is concerned, a milestone theorem was proven by S. Lloyd in 1996 ([30]). Its statement reads as follows: the complicated many-body dynamics of a local Hamiltonian can be efficiently simulated inducing on a controllable quantum system a reduced number of elementary time-evolutions to be engineered from outside. This digital quantum simulator is said to be universal, since, once reprogrammed, it allows for the simulation of an arbitrary local Hamiltonian.

Unfortunately, the difficulty of realizing such a powerful experimental plat-

form forces the formulation of a less demanding but still ambitious concept, traditionally referred to as analog quantum simulator. The latter is a purpose-built setup whose range of applicability is limited to the quantum simulation of a limited class of theoretical models.

General and overall accepted criteria to answer the question whether a given quantum system can be exploited for quantum simulation purposes have not been formulated yet, but some key properties to be fulfilled can be anyway identified. In first instance, the microscopic theoretical knowledge of the system must be detailed enough to allow for the understanding of the simulation with an $ab-initio$ approach. Additionally, the system must contain a large number of elementary constituents, since the ultimate goal of quantum simulation is the efficient study of many-body physics, and the experimentalist is expected to be able to manipulate it by, e.g., varying the couplings between its constituent units and initializing it in a range of different initial states, as the concept of simulation itself implies. Finally, the desired information should be extracted from the setup via a measurement of the system, carried out with high fidelity.

Many possible realizations of a quantum simulator have been proposed and explored with the help of cold atoms in optical lattices, trapped ions, photons, superconducting circuits and arrays of quantum dots. The physical units employed in quantum simulation setups we will focus on are the well known Rydberg atoms.

These represent highly excited atoms where one electron occupies a high principal quantum number n state, such that it spends statistically most of its time far away from the atomic nucleus, thereby permitting a description of their properties by means of a hydrogen-like picture. The huge dipole operator matrix elements emerging from their quantum-mechanical characterization makes them extremely sensitive to the presence of external electromagnetic fields and is responsible for the strong dipole-dipole interaction among Rydberg atoms, whose characteristic order of magnitude is overwhelmingly larger than the standard induced dipole-induced dipole van der Waals interaction between neutral atoms in their ground state configurations, as it can be shown to scale as n^4 (see [31]). In order to complete the phenomenological characterization of Rydberg states, let us mention the Rydberg excitation blockade effect: when an atom is excited to a Rydberg state, the Rydberg excitation of other atoms separated from the excited one by a characteristic distance R_b, called blockade radius, is strongly inhibited by virtue of the atomic energy level shift induced by the strong interatomic interaction.

Their susceptibility to be employed for quantum simulation purposes originates in first instance from the observation that the most fundamental requirement for the excitation of atomic systems to Rydberg states is a technologically accessible laser driving of an ultracold atomic gas trapped in an optical lattice. Apart from the latter, purely technical argument, Rydberg atoms raise additional scientific interest in view of the long-range interaction properties they display, which are expected to represent the key ingredient to the foundation of the realm of the highly controlled quantum simulation of long-range interacting systems.

2.2 Quantum simulation with Rydberg atoms

As briefly discussed in the precedent section, Rydberg atoms are particularly well suited for the purpose of simulating long-range interacting systems and have been therefore extensively studied in the framework of quantum simulation. A first, pioneering paper which points out that neutral atoms excited to Rydberg states are a promising platform for quantum simulation and quantum information processing is [26].

The authors, who already envisioned the realization of quantum simulation setups inspired by their work, devoted their attention to the experimental characterization of a two-dimensional gas of alkali atoms trapped in a rotationally invariant harmonic confinement potential and pinned in a square optical lattice. The atoms, initially in their ground state energy level, are resonantly coupled to a Rydberg state, so that the Hamiltonian governing the dynamics of the system takes the form:

$$H = \frac{\hbar\Omega}{2} \sum_j \left(|g_j\rangle\langle r_j| + |r_j\rangle\langle g_j| \right) + \sum_{i<j} V_{ij} n_i n_j \tag{2.1}$$

having denoted the ground state at site j as $|g_j\rangle$, the Rydberg state at site j as $|r_j\rangle$ and the projector $|r_j\rangle\langle r_j|$ onto the Rydberg state at site j as n_j. The Rabi frequency associated to the coherent coupling of the ground and excited states is indicated as Ω, whereas the repulsive van der Waals potential between two Rydberg atoms takes the asymptotic form $V_{ij} \propto |i-j|^{-6}$.

The description of the strongly correlated excitation dynamics of a resonantly driven Rydberg gas yields the emergence of spatially ordered excitation patterns in the high-density components of the prepared many-body state. These form mesoscopic crystals of Rydberg excitations with random orientation but well defined geometry, which demonstrate the potential of Rydberg gases to give rise to exotic phases of matter, thereby suggesting that they can serve as a basis for the quantum simulation of long-range interacting models.

On the other hand, one of the studies which give direct evidence of the scientific relevance of Rydberg atom quantum simulators with programmable interactions is presented in [28], where such an experimental platform is realized and employed to characterize the quantum critical dynamics associated to the quantum phase transitions occurring in the model defined by the Hamiltonian:

$$H = \frac{\Omega}{2} \sum_j \left(|g_j\rangle\langle r_j| + |r_j\rangle\langle g_j| \right) - \Delta \sum_j n_j + \sum_{i<j} V_{ij} n_i n_j \tag{2.2}$$

where $n_j = r_j\rangle\langle r_j|$ is the projector onto the Rydberg state at site j, Δ and Ω are the detuning and Rabi frequency of the coherent laser coupling between the ground state $|g\rangle$ and the Rydberg state $|r\rangle$, and V_{ij} is the interaction strength between atoms in the Rydberg state at sites i and j, which decays as $|i-j|^{-6}$. The experimental system described by (2.2) is realized by a reconfigurable one-dimensional array of ^{87}Rb atoms with tunable interactions.

Their investigation proceeds by noticing that, while the condition $\Delta < 0$ enforces a many-body ground state in which all atoms occupy the ground state $|g\rangle$, for $\Delta > 0$ the competition between the detuning term, which favors a large Rydberg fraction, and the Rydber blockade mechanism, which prohibits the simultaneous excitation of atoms within a characteristic length scale called blockade radius, gives rise to a rich variety of spatially ordered ground state configurations separated by quantum phase transitions.

By studying the growth of spatial correlations while crossing the corresponding phase diagrams, the authors achieve ambitious goals such as the exploration of scaling universality and the experimental verification of the quantum Kibble-Zurek mechanism, whose classical counterpart describes nonequilibrium dynamics and the formation of topological defects in a second-order phase transition driven by thermal fluctuations, for an Ising-type quantum phase transition.

A further noticeable effort in the field of quantum simulation is represented by the results shown in [11], which offer great insights into the extraordinary opportunities offered by such an approach to the many-body problem. Indeed, their work exploited the deterministic preparation of a 51-atom array and the coupling of neutral atoms to highly excited Rydberg states to simulate a very general model Hamiltonian of the form:

$$\frac{H}{\hbar} = \sum_i \frac{\Omega_i}{2}\sigma_x^i - \sum_i \Delta_i n_i + \sum_{i<j} V_{ij} n_i n_j \tag{2.3}$$

where $n_i = |r_i\rangle\langle r_i|$, $\sigma_x^i = |r_i\rangle\langle g_i| + |g_i\rangle\langle r_i|$ and $|r_i\rangle$ and $|g_i\rangle$ represent respectively the ground state and the Rydberg state of the atom sitting at position i. The parameters of the model depend on the frequency of the lasers driving the atomic excitations of the elementary constituents of the setup and on the energy spectrum of the atomic systems.

Thanks to the aforesaid experimental platform, the remarkable achievement of observing various phase transitions to spatially ordered states that break different discrete symmetries has been accomplished, allowing for the detailed description of the phase diagram of the model defined by (2.3) as a function of the interaction range. Furthermore, the authors of [11] turn out to be able to characterize the dynamics of the system after a quantum quench across a phase boundary, thereby monitoring, e.g., the density of domain walls separating spatially ordered configurations, as better discussed in figure (2.1).

A fascinating work with the purpose of improving the performances of quantum simulation platforms based on Rydberg gases is presented in [8], where the authors propose an innovative paradigm for the quantum simulation of spin Hamiltonians based on the so called circular Rydberg atoms. Among their main distinctive features, it is useful to recall that their outer electron occupies a state of maximum angular and orbital quantum numbers, i.e. $l = |m| = n-1$, and the corresponding electronic wavefunction resembles a thorus of major radius $R_n = a_0 n^2$ and thickness dispersion $\frac{\Delta r}{r} \sim \frac{1}{\sqrt{2n}}$, representing therefore the closest analogue of a semiclassical orbit of the Bohr-Sommerfeld model in a rigorously quantum treatment.

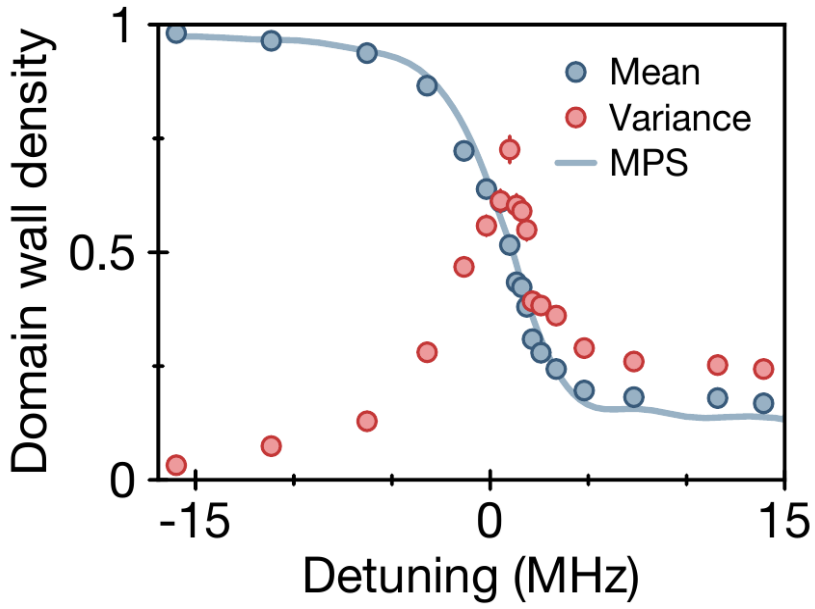

Figure 2.1: The transition into a spatially ordered configuration where subsequent atoms in the 1D array alternate between Rydberg and ground state is characterized by computing mean and variance of the domain wall density while varying the control paramenter across the phase boundary. As the system enters the ordered phase, the ordered domains grow in size, leading to a substantial reduction in the domain wall density. The experimental data points show a nice agreement with the outcome of matrix product state simulations with the same setting as the performed experiments. On the other hand, the peak in the variance of the domain wall density signals the presence of domains with fluctuating lengths at the transition point, consistently with the expectation of a scale-free behaviour of the system at criticality. The figure is taken from [11].

The $n = 50$ resp. $n = 48$ circular levels of a given species of Rydberg atoms allow to treat the elementary constituents of the quantum simulator as effective spin-$\frac{1}{2}$ systems, while the dipole-dipole interactions provide with a spin-$\frac{1}{2}$ XXZ chain Hamiltonian, defined by the relation:

$$\frac{H}{h} = \frac{\Delta^{'}}{2}(\sigma_1^z+\sigma_N^z)+\frac{\Delta}{2}\sum_{j=2}^{N-1}\sigma_j^z+\frac{\Omega}{2}\sum_{j=1}^{N}\sigma_j^x+\sum_{j=1}^{N-1}\left[J_z\sigma_j^z\sigma_{j+1}^z+J(\sigma_j^x\sigma_{j+1}^x+\sigma_j^y\sigma_{j+1}^y)\right] \tag{2.4}$$

and whose parameters can be tuned at will over a wide range of values by manipulating control electromagnetic fields. The whole simulation platform is placed in between the two parallel plates of a capacitor hosting no field modes with a frequency close to the one associated to the spontaneous emission decay channel of the circular levels involved in the proposed quantum simulator design,

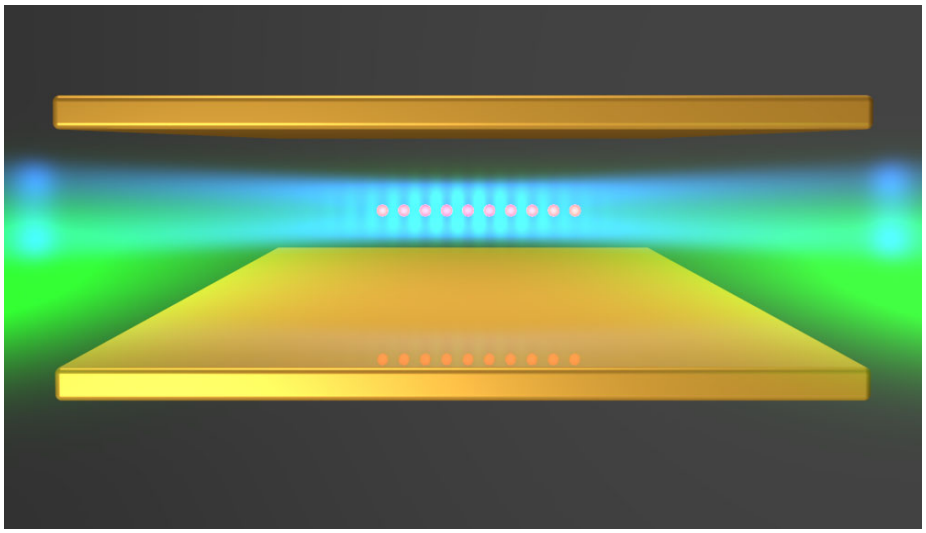

Figure 2.2: Pictorial representation of the proposed circular-state quantum simulator. The figure is taken from [8].

thereby increasing their characteristic lifetime. The latter, intrinsically longer in the case of laser-trapped circular atoms with respect to non-circular states and combined with the inhibition of their microwave spontaneous emission and their low sensitivity to collisions and photoionization, make trapping lifetimes in the minute range realistic with state-of-the-art techniques.

Finally, as a technical remark, the realization of quantum simulators requires high-level technical prerequisites ensuring the high-fidelity preparation of the system in a given state and the fine tuning of the interatomic interactions. Such goals are only achieved by implementing an experimental platform with an outstanding level of precision in the atomic positioning and an excellent degree of isolation, which allows for the investigation of nonequilibrium phenomena one cannot access in traditional condensed matter settings.

As a consequence, the opportunity of increasing the accuracy in the simultaneous control over many quantum objects has been explored by a rich variety of experimental groups. A representative study in this direction is the one presented in [9], where Barredo et al. demonstrate how to prepare user-defined geometric configurations of the ultracold atoms under analysis starting from a stochastically-loaded array of traps with the help of rapidly moving optical tweezers under real-time control.

Since the problem of finding the optimal sequence of moves which minimizes the time it takes to reorder the initial, random configuration into the target one is a hard computational task, the authors developed a heuristic path-finding algorithm which results in $\sim \frac{N}{2}$ required moves, where N is the number of trapped atoms. The typical times needed to complete the procedure for the

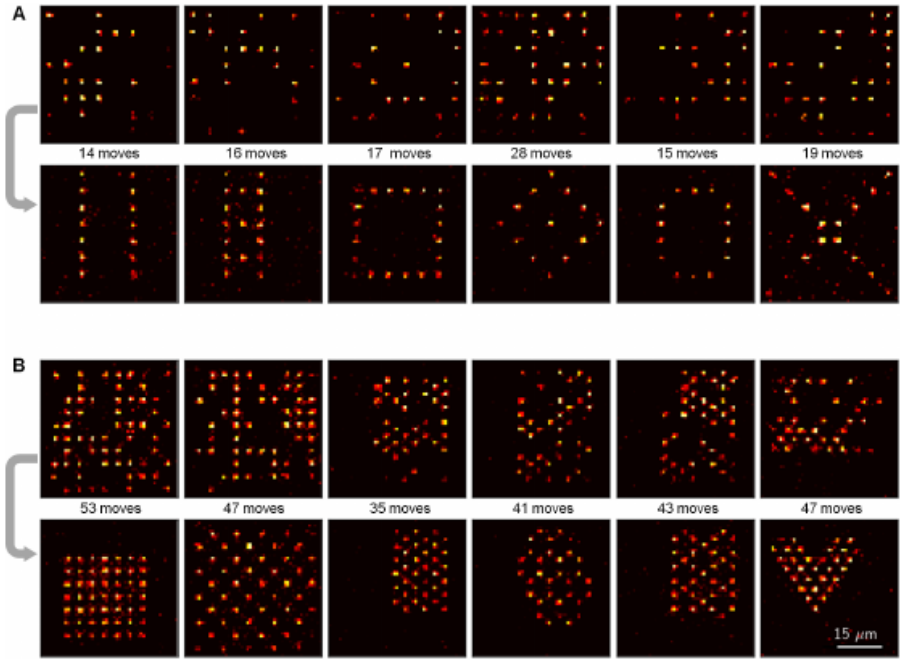

Figure 2.3: Gallery of user-defined geometries (bottom images) obtained from the initial, random configurations (top images). The number of elementary moves needed to achieve the sorting is also indicated. The figure is taken from [9].

largest arrays at their disposal ($N \sim 50$ atoms) turned out to require less than $50ms$, which represents a timescale still shorter than the lifetime of the initial configuration. A gallery of user-defined geometries together with the initial randomly loaded arrays from which these are obtained is shown in figure (2.3).

2.3 Phase diagram of the half-filled $t - U_1 - U_2$ model

Motivated by the recent experimental efforts in the study of lattice systems characterized by dipole-dipole interactions, the purpose of this thesis is to study one-dimensional systems with long-range interactions. We will mostly use a fermionic notation, but, thanks to the Jordan-Wigner transformation, our results can be easily transferred to the spin language that is most appropriate for the discussion of arrays of Rydberg atoms. We are now ready to tackle the problem of investigating the zero-temperature phase diagram of the following model Hamiltonian in half-filling conditions:

$$H = -t \sum_i \left[c_i^\dagger c_{i+1} + h.c. \right] + U_1 \sum_i n_i n_{i+1} + U_2 \sum_i n_i n_{i+2} \tag{2.5}$$

where the creation and annihilation operators obey canonical anticommutation relations, i.e.:

$$\{c_i, c_j^\dagger\} = \delta_{ij} \tag{2.6}$$

$$\{c_i, c_j\} = \{c_i^\dagger, c_j^\dagger\} = 0 \tag{2.7}$$

and t represents the hopping amplitude between neighbouring sites, while $U_1 \geq 0$ and $U_2 \geq 0$ give rise to repulsive nearest-neighbour and next-to-nearest-neighbour density-density interactions, respectively. The phase diagram of the model, whose recharacterization will be the main focus of many subsequent efforts of the current thesis work, has already been proposed on purely numerical grounds in [2], where density matrix renormalization group (DMRG) simulations have been performed in order to determine an accurate picture of the different phases emerging from the interplay between the Hamiltonian parameters.

2.3.1 Phases and order parameters

The final result of the investigations in [2] is shown in figure (2.4).

The model exhibits four distinct phases: the Luttinger liquid (LL), the (•○) charge-density wave (CDW-I), the (••○○) charge-density wave (CDW-II) and the bond-order (BO) phases. Here, the black dot has been used with the meaning of an occupied site, whereas the white dot is associated to an empty one.

Before moving on to the summary of the technical aspects that are necessary to discriminate the aforementioned phases, a first quick look at the phase diagram shows its consistency with the naive physical intuitions that one may have about it: in particular, one might expect that, when either U_1 or U_2 is much larger than the other parameters of the model, then the energy minimization task is achieved by rearranging the fermions in the charge-ordered configuration which allows to remove the contribution of the dominant interaction to the energy of the associated ground state. On the other hand, it is equally reasonable, at least on a purely intuitive level, that the system will settle down to a liquid phase with prevailing kinetic fluctuations in the case of interaction strengths U_1 and U_2 whose value is negligible with respect to the hopping amplitude parameter t.

LL to CDW-I transition

Formally speaking, the richness of the phase diagram in figure (2.4) requires a hard technical work in order to obtain a proper description of it. We begin the analysis with the study of the transition from the LL phase to the CDW-I phase, which is in first instance signaled by a finite non-zero value in the

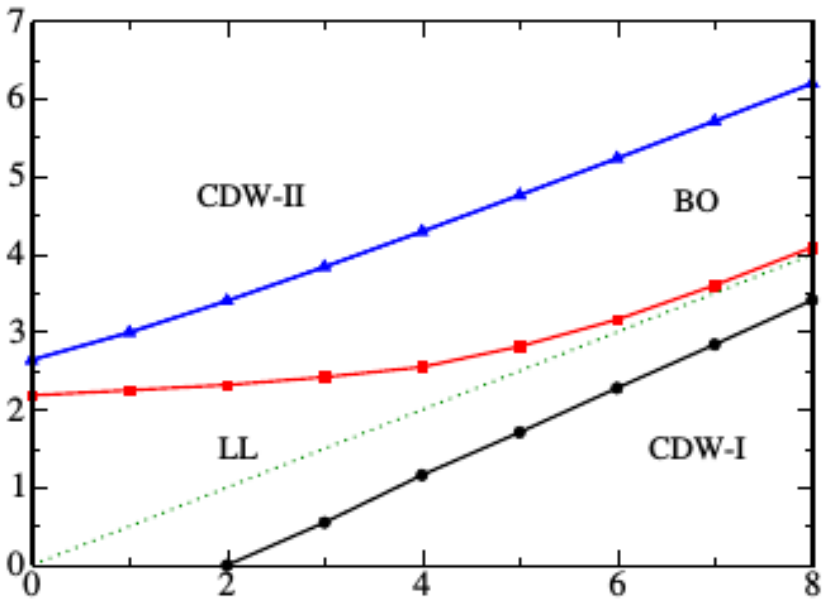

Figure 2.4: Phase diagram of the half-filled $t - U_1 - U_2$ model as proposed in [2].The hopping amplitude has been set to $t = 1$. The figure is taken from [2].

thermodynamic limit of the structure factor $S(k = \pi)$, defined in its generality by the formula:

$$S(k) = \frac{1}{L^2} \sum_{l,j} e^{ik(l-j)} \left(\langle n_l n_j \rangle - \langle n_l \rangle \langle n_j \rangle \right) \tag{2.8}$$

The latter has been evaluated at the wavevector associated to the characteristic spatial modulation of the density profile. The result, shown in figure (2.5), provide evidence for the emergence of charge order across the LL-CDW-I phase boundary, even though the precise location of the transition point turns out to be unfeasible with such a characterization procedure.

Further refinements on the precise determination of the phase boundary between the two aforesaid phases are better achieved by introducing the single-particle excitation gap $\Delta(N, L)$, defined by the relation:

$$\Delta(N, L) = E(N + 1, L) + E(N - 1, L) - 2E(N, L) \tag{2.9}$$

where $E(N, L)$ indicates the ground state energy of the model with N particles on al lattice of length L. Then, a more precise characterization of the phase boundary between the LL phase and the CDW-I phase is recovered through the analysis of the exponential opening of a non-zero single-particle excitation gap in the CDW-I phase, as predicted from the observation that such a transition is known to belong to the Berezinskii-Kosterlitz-Thouless (BKT) universality

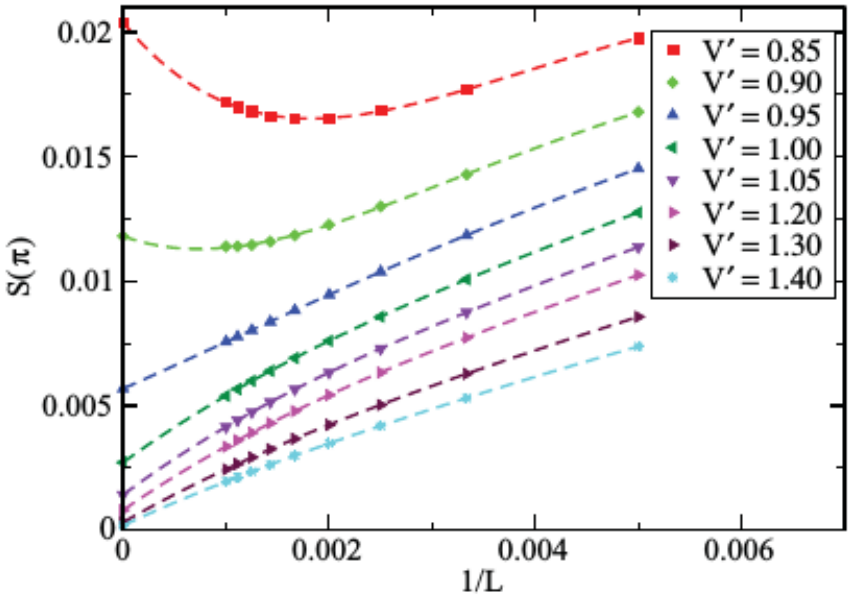

Figure 2.5: Finite-size scaling of $S(\pi)$ for different values of U_2, for $U_1 = 4$, across the CDW-I to LL phase.The figure is taken from [2].

class, combined with the use of a finite-size-scaling relation for the very same quantity. Interestingly, as the phase diagram proposed in figure (2.4) shows, by increasing the value of U_2 to strictly positive values, the transition point from the LL phase to the CDW-I phase is shifted to higher values of U_1, consistently with the expectation that the competition between the charge orders favored by the two interactions terms stabilizes the liquid phase through a gain in kinetic fluctuations.

LL to BO phase transition

Moving on to the characterization of the transition from the LL phase to the BO phase, the relevant observable turns out to be the so called BO parameter, defined through the relation:

$$O_{BO} = \frac{1}{L}\sum_i (-1)^i \left[\langle c_i^\dagger c_{i+1} + h.c.\right] \tag{2.10}$$

with the goal of measuring the local kinetic energy inhomogeneities and the dimerization level of the system. By crossing the corresponding phase boundary, the finite-size scaling of the BO parameter is employed in order to roughly locate the transition point, as reported in figure (2.6). As in the previous case, predictions obtained by means of a finite-size-scaling relation for the gap in the

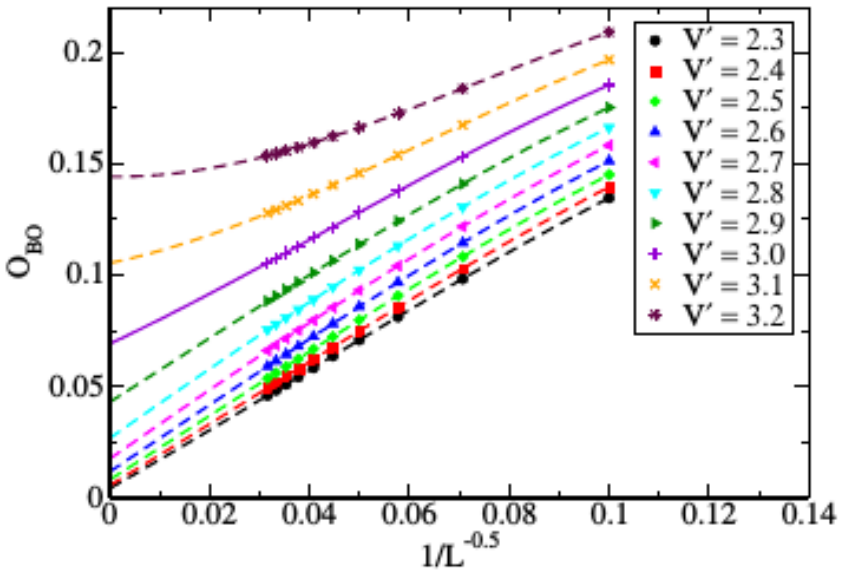

Figure 2.6: Finite-size scaling of O_{BO} for different values of U_2, for $U_1 = 4$, across the LL to BO phase.The figure is taken from [2].

single-particle excitation spectrum support the findings obseerved by looking at the extrapolated value of the BO parameter. Interestingly, as unveiled by the phase diagram of the model in figure (2.4), when a strictly positive value of U_1 is superimposed to the system, it starts competing with the bond-ordering induced by the presence of U_2, hence resulting in a stabilization of the LL phase up to a larger critical value of U_2 with respect to the one observed in absence of the nearest-neighbour density-density interaction, i.e. $U_1 = 0$.

BO to CDW-II phase transition

Finally, the transition from the BO phase to the CDW-II phase is formally described by the emergence of a finite non-zero value of $S(\frac{\pi}{2})$ in the extrapolation to the thermodynamic limit, as expected from the wavelength associated to the spatial density modulation of the CDW-II. The corresponding results, displayed in figure (2.7), are again complemented with a more sophisticated analysis based on scaling theory for $S(\frac{\pi}{2})$, thereby obtaining numerical evidence that the critical exponents found at the critical point belong to the 2D universality class.

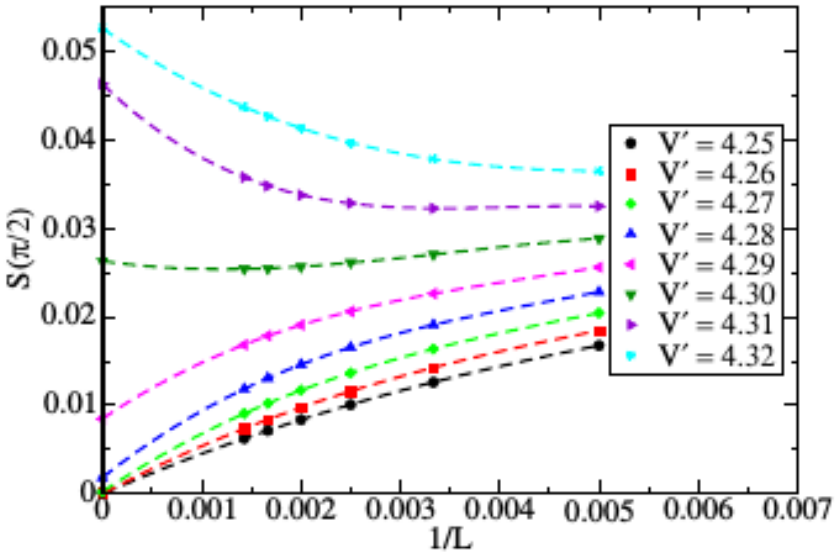

Figure 2.7: Finite-size scaling of $S(\frac{\pi}{2})$ for different values of U_2, for $U_1 = 4$, across the BO to CDW-II phase.The figure is taken from [2].

2.4 Longer-range interactions

2.4.1 Model and motivations

The work presented in [4] represents a research effort in the further development of the current understanding of one-dimensional fermionic physics. The authors of the paper aim at a comprehensive investigation of the rich phase diagram emerging in presence of competing finite-range interactions together with kinetic energy fluctuations. In order to achieve such an ambitious goal, the focus of their investigation are one-dimensional fermionic models with even longer-range interaction contributions with respect to the ones included in [2]. The scenarios emerging from their numerical results imply the appearance of direct transitions between different charge orders, as well as mediating liquid behaviour in between the insulating regions of the phase diagram. The investigations are based on a model of spinless fermions on a lattice of size L interacting through a finite-range repulsive potential of maximal range p. The Hamiltonian of the model is written as:

$$H = -t \sum_i \left[c_i^\dagger c_{i+1} + h.c. \right] + \sum_i \sum_{m=1}^{p} U_m n_i n_{i+m} \tag{2.11}$$

where $c_i, c_i^\dagger$ are fermionic creation and annihilation operators, $n_i = c_i^\dagger c_i$, t is the hopping amplitude and U_m gives the interaction energy contribution for

GS unit cell	Energy density	f
	$p = 2, Q = 1/2$	
●○	$U_2/2$	2
●●○○	$U_1/4$	4
	$p = 4, Q = 1/2$	
●○	$(U_2 + U_4)/2$	2
●●○○	$(U_1 + U_3 + 2U_4)/4$	4
●●●○○○	$(2U_1 + U_2 + U_4)/6$	6
●●●●○○○○	$(3U_1 + 2U_2 + U_3)/8$	8
●○○●○●●○	$(U_1 + 2U_2 + 3U_3)/8$	8

Figure 2.8: Ground state unit cells and corresponding energy content in the atomic limit of half-filled systems with interaction range $p = 2$ and $p = 4$. The degeneracy f accounts for the translational freedom of each charge-ordered phase.The figure is taken from [4].

particles that are m sites apart.

2.4.2 Classification and phenomenological characterization

The starting point of the analysis relies on the systematic classification of the allowed charge-ordered configurations as a function of the interaction range p and of the available commensurable particle densities in the atomic limit, i.e. when $t = 0$. In such a case, the derivation of the form of the ground state configuration is entirely based on combinatorial energetic considerations, shows abrupt transitions between the different insulating phases and gives results such as the one displayed in figure (2.8).

The characterization of the system at finite kinetic energy, where the transitions can be mediated by liquid and BO phases, as observed in the $t - U_1 - U_2$ model, proceeds with the help of DMRG simulations. With particular reference to the results found in [4] for the $t - U_1 - U_2$ model at half-filling, which is the one of interest for the purpose of the current thesis work, the authors examine the behaviour of the fermionic system for $U_1 = 10$, $t = 1$ and varying U_2. The findings are consistent with previous works on the very same model and show the well known transition from the (●○) configuration to the (● ● ○○) one, mediated by the emergent LL and BO phases.

Armed with the goal of summarizing the technical expedients employed in getting to such results, it is worth mentioning in the first place that the aforesaid phases are discriminated on a purely phenomenological level by looking at the kinetic energy density T and the BO parameter O_{BO}, defined respectively as:

$$T = \frac{1}{L}\sum_i \langle c_i^\dagger c_{i+1} + h.c.\rangle \tag{2.12}$$

$$O_{BO} = \frac{1}{L}\sum_i (-1)^i \langle c_i^\dagger c_{i+1} + h.c.\rangle \tag{2.13}$$

Figure (2.9) shows that, while the kinetic energy profile only captures the transition from the BO phase to the ($\bullet\bullet\circ\circ$) phase through a discontinuity in its first derivative, the BO parameter captures all three transitions, carrying hence in this case more information. In particular, even though the BO parameter vanishes in the thermodynamic limit both in the LL phase and in the ($\bullet\circ$) phase, its different scaling with increasing bond dimension of the DMRG simulation in the two phases still allows to discriminate them. Furthermore, in order to achieve a more detailed description of the aforementioned phases, the density-density correlation function is introduced:

$$N_m = \frac{1}{L}\sum_i \langle n_i n_{i+m}\rangle \tag{2.14}$$

so that it is possible to probe the emergence of ordering phenomena in the system. Indeed, by introducing the extrapolated correlator:

$$\lim_{k\to+\infty} N_{m+kP} = N_m^\infty, \;\; m = 1, \ldots, P \tag{2.15}$$

where P is the largest unit-cell size among the ones exhibited by the different charge orders of the model, long-range ordering effects can be detected. As shown in figure (2.10), it is noticeable that all charge-ordered configurations are indeed captured by looking at the behaviours of the extrapolated correlators in a way consistent both with the naive expectation of their values solely based on the ground state configuration and with the results obtained from the analysis of the kinetic energy density and the BO parameter. Finally, one should recognise that such an observable cannot be employed to discriminate between the LL phase and the BO phase, since in liquid-like phases the extrapolated correlators are easily seen to become trivial, as shown by the following trivial computation:

$$\lim_{k\to+\infty} N_{m+kP} = \lim_{k\to+\infty} \frac{1}{L}\sum_i \langle n_i n_{i+m+kP}\rangle \tag{2.16}$$

Since $\langle n_i n_{i+r}\rangle \approx \langle n_i\rangle\langle n_{i+r}\rangle$ for large values of r and by using $\langle n_i\rangle = \frac{1}{2}$ at half-filling in a liquid phase, then the extrapolated correlators are easily seen to take the value:

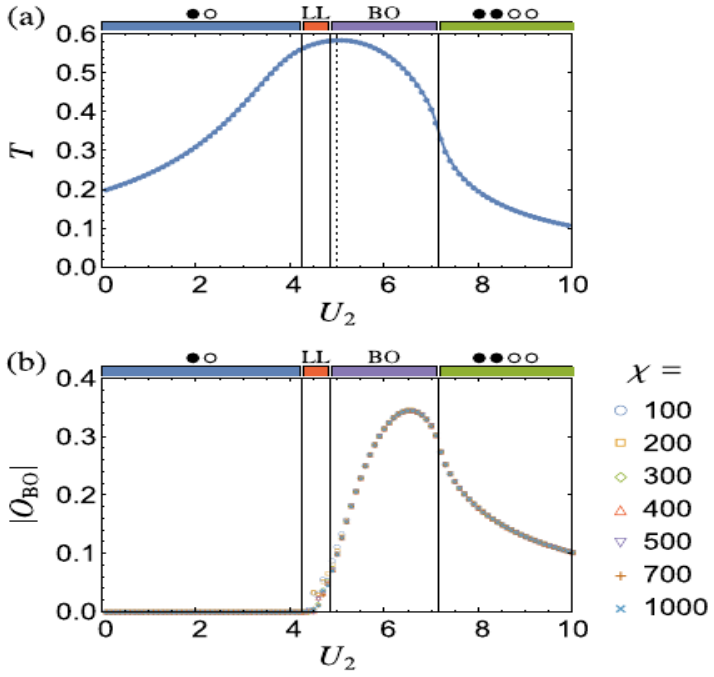

Figure 2.9: Phenomenological signatures of phases and transitions in the kinetic energy density and BO parameter for the model (2.11) in half-filling conditions with $t = 1, U_1 = 10$ and varying U_2. χ denotes the bond dimension in the corresponding DMRG simulation.The figure is taken from [4].

$$N_m^{\infty} = \frac{1}{4} \tag{2.17}$$

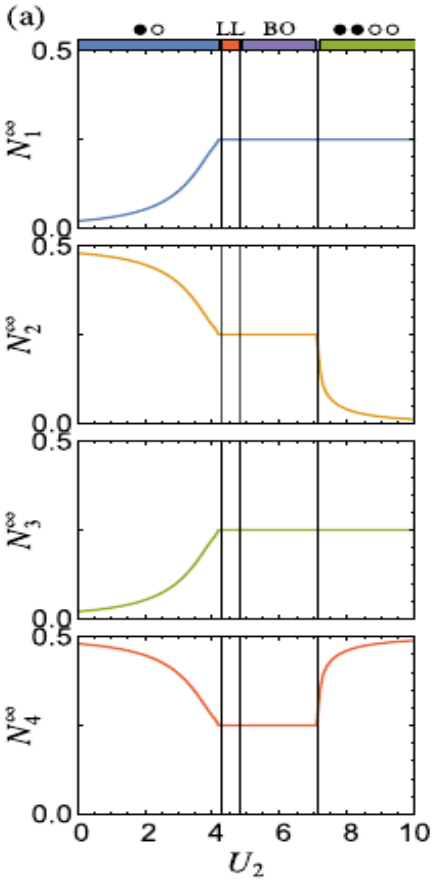

Figure 2.10: Extrapolated correlators N_m^∞ for $p = 2$ and system parameters as in figure (2.9).The figure is taken from [4].

Chapter 3

Review of bosonization

3.1 Introduction and bibliographic references

The goal of the present chapter is the presentation of the most crucial informations concerning the bosonization technique, whose intensive and successful application to the theoretical characterization of the phases and the critical properties of one-dimensional (1D) systems make it an essential tool to their analysis. The subsequent material has no claim of originality and has become by now standard textbook material. The main sources of knowledge I have been employing are [1], [12], [13] and [15], together with unpublished lecture notes kindly made available by prof. G. Roux. The motivated reader is invited to refer to the aforementioned material if interested in further and more detailed discussions and calculations.

3.2 Conceptual framework

The key idea of the bosonization technique is the construction of an effective low-energy field theory for 1D strongly correlated fermionic many-body systems with quartic interaction terms in the associated second-quantized Hamiltonian. Since the model Hamiltonian cannot be easily diagonalized through standard techniques in such settings, the bosonization prescription aims to reexpress the fermionic degrees of freedom in terms of appropriate bosonic fields, which allow for a more convenient representation of the system.

The starting point of the standard scenario used to introduce bosonization is the following model Hamiltonian:

$$H = H_0 + H_U \tag{3.1}$$

where:

$$H_0 = -t \sum_i [c_i^\dagger c_{i+1} + h.c.] \tag{3.2}$$

is the kinetic energy term associated to the hopping processes between neighbouring sites and H_U represents the contribution coming from the interactions between the fermions, whose strength is parametrized by the energy scale U. The model is defined on a 1D lattice of L sites and periodic boundary conditions are considered, i.e. $c_{j+L} = c_j$. For the sake of completeness, the $c_j, c_j^\dagger$ are fermionic creation and annihilation operators and obey the following canonical anticommutation relations:

$$\{c_i, c_j^\dagger\} = \delta_{ij} \tag{3.3}$$

$$\{c_i, c_j\} = \{c_i^\dagger, c_j^\dagger\} = 0 \tag{3.4}$$

In the limit where $U = 0$, the interaction term vanishes and one is left with the free Hamiltonian H_0, which can be easily diagonalized by means of Fourier transformation, defined by the following relation :

$$c_k := \frac{1}{\sqrt{L}} \sum_{j=1}^{L} c_j e^{-ikj} \tag{3.5}$$

with inverse transformation:

$$c_j := \frac{1}{\sqrt{L}} \sum_{k} c_k e^{ikj} \tag{3.6}$$

where L represents the number of sites and, supposing to work with periodic boundary conditions, the sum over k runs over the associated first Brillouin zone, defined by :

$$k = \frac{2\pi}{L} n \tag{3.7}$$

with n given by:

$$n = -\frac{L}{2}, -\frac{L}{2} + 1, \ldots, \frac{L}{2} - 1 \tag{3.8}$$

assuming an even number of sites . After such a transformation, the Hamiltonian takes the diagonal form :

$$H_0 = -2t \sum_{k} \cos(k)\, c_k^\dagger c_k \tag{3.9}$$

The ground state will then be represented by a Fermi sea, in which all the lowest energy states will be occupied up to the energy level E_F, known as Fermi energy.

When turning on the interaction term, one may suppose on an intuitive and purely qualitative level that, at least in the perturbative regime $U \ll t$, only the low energy excitations involving states lying very close to the Fermi points are expected to occur in the dynamical evolution of the system. Hence, since we expect to deal mainly with scattering events around the Fermi points, it looks natural to linearize the dispersion relation around the Fermi momenta

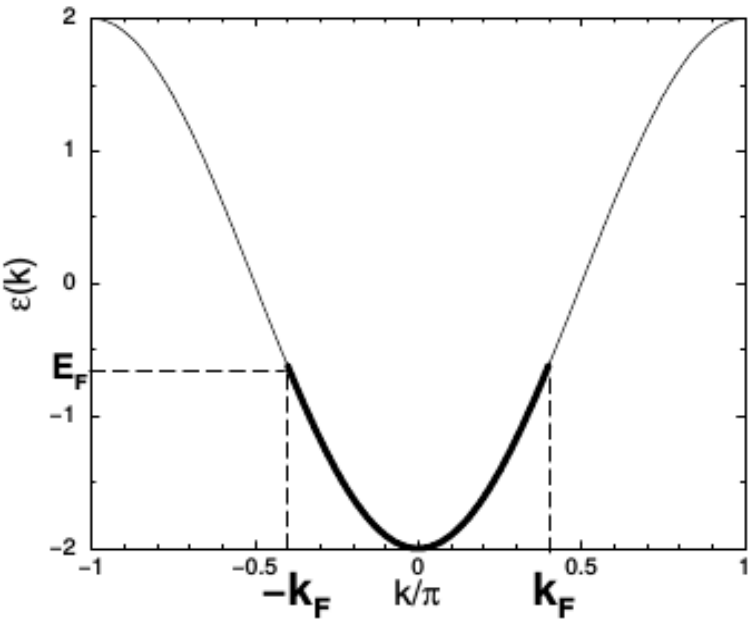

Figure 3.1: Non-interacting Fermi sea.The image shows a pictorial representation of the ground state configuration, where the lowest energy states of the system are filled up to the so called Fermi momentum k_F, whose value depends linearly on the fermionic density in the system. The corresponding energy $E_F = E(\pm k_F)$ is known as Fermi energy. The image is taken from [12].

and, consequently, to extend the linear approximation to the whole real axis, which amounts to taking an appropriate continuum limit and turns out to be mathematically convenient to make further progress. By such a procedure, it is meant that the linearized version of the dispersion relations around the Fermi points replaces the original form of the spectrum in an effective way and is now defined over the set $\{k_n = \frac{2\pi}{L} n \mid n \in \mathbb{Z}\}$, thus extending to the entire real axis and amounting to taking the limit of infinite number of sites while sending the lattice spacing to zero, so that the (finite) length of the system is kept constant.

3.3 Effective field theory formulation

3.3.1 Hilbert space

Having introduced an infinite number of degrees of freedom, we have effectively switched to a field-theoretical description where the Hilbert space is defined as

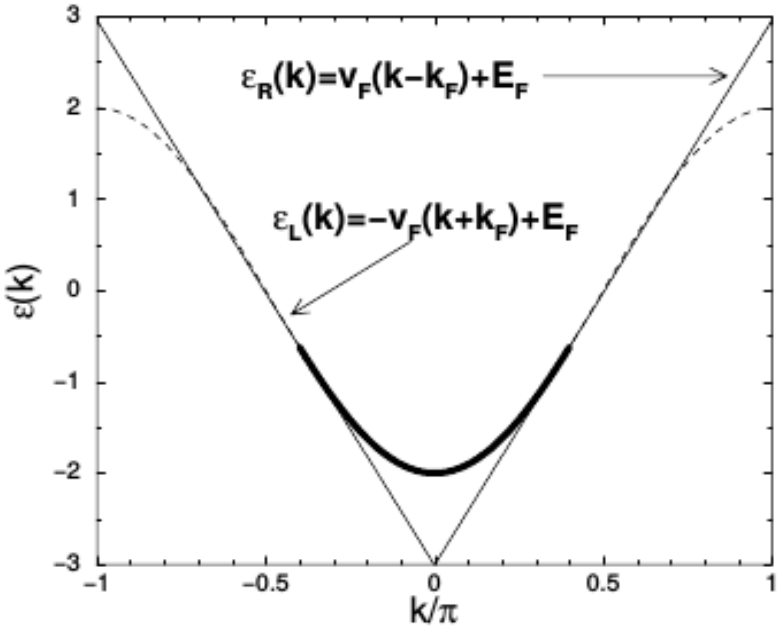

Figure 3.2: Linearization of the spectrum around the Fermi points.Since the only relevant scattering events take place close to the Fermi points, one may equivalently study the properties of the effective linear dispersion model shown in figure. The increasing branch of the spectrum is called right-moving branch, while the decreasing one is referred to as left-moving branch, with reference to the orientation of the mean velocity of the fermions occupying the corresponding energy states. The figure is taken from [12].

the Fock vector space spanned by all states generated through the action of a finite number of creation and annihilation operators c_k and $c_k^\dagger$ on the vacuum state, in which all states up to the Fermi energy are occupied. From now on, unless in case of explicit reference to a different framework, all results will be derived for the case of a right-moving branch of the spectrum, but the generalization to the case of left-moving branches turns out to be pretty straightforward.

Formally, the vacuum state $|0\rangle_0$ of the branch is defined by the relations:

$$c_k|0\rangle_0 = 0, \;\; k > 0 \tag{3.10}$$

$$c_k^\dagger|0\rangle_0 = 0, \;\; k \leq 0 \tag{3.11}$$

where the wavevector belongs to the set $\{k_n = \frac{2\pi}{L}n \mid n \in \mathbb{Z}\}$ (resulting from the continuum limit in the finite interval $\left[-\frac{L}{2}, \frac{L}{2}\right)$ in a real space formulation) and has been appropriately shifted in such a way that the Fermi level intersects the dispersion relation at $k = 0$.

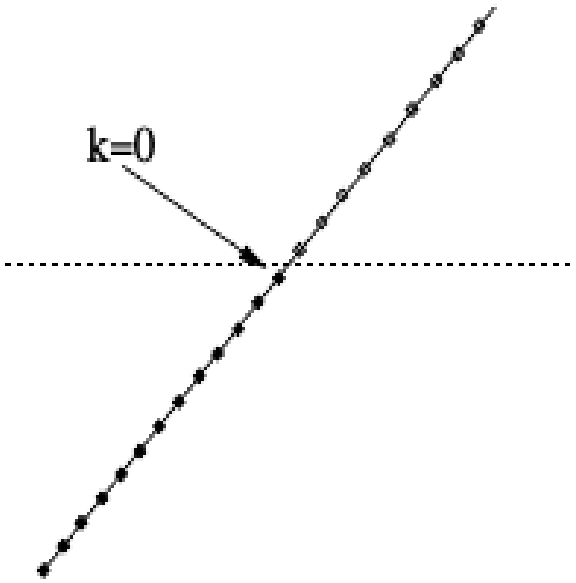

Figure 3.3: Vacuum state of the right-moving branch as defined by the equations (3.10) and (3.11). Figure from [12].

The Fock space of the many-body problem can then be formally decomposed as a direct sum of Hilbert spaces with fixed particle number. Such a quantum number is defined in terms of its deviation from the one computed in the vacuum state as:

$$N := \sum_k \left[c_k^\dagger c_k - \langle c_k^\dagger c_k \rangle_0 \right] = \sum_k : c_k^\dagger c_k : \tag{3.12}$$

where the normal-ordered version of a string of creation and annihilation operators $ABCD$ has been denoted by $: ABCD :$ and is defined by the operation of moving all operators that destroy the vacuum state to the right of the expression while multiplying by -1 at each transposition, which is equivalent to the subtraction of the vacuum expectation value of the very same operator in the case of products of two fermionic operators.

The N-particle Hilbert space H_N is then equipped with a corresponding N-particle ground state $|N\rangle_0$, generated by adding N fermions on top of the vacuum state $|0\rangle_0$ in case of positive N and by removing the N highest energy fermions from the vacuum state in case of negative N, and is spanned by the states resulting from the application of a finite number of particle-hole excitations to $|N\rangle_0$.

3.3.2 Density fluctuation operators

A key role in the bosonization formalism will be played by the so called density fluctuation operators, which are defined as follows:

$$\rho(q) = \sum_k c^+_{k+q} c_k \tag{3.13}$$

with $q \neq 0$.

In order to understand the framework they originate from, we introduce the fermionic field operator:

$$\psi(x) = \frac{1}{\sqrt{L}} \sum_k c_k e^{ikx} \tag{3.14}$$

satisfying canonical anticommutation relations over the interval $\left[-\frac{L}{2}, \frac{L}{2}\right)$, i.e.:

$$\{\psi(x), \psi^\dagger(x')\} = \delta(x - x') \tag{3.15}$$

$$\{\psi(x), \psi(x')\} = \{\psi^\dagger(x), \psi^\dagger(x')\} = 0 \tag{3.16}$$

whenever $x, x' \in \left[-\frac{L}{2}, \frac{L}{2}\right)$. The convenience of such a mathematical object will emerge as it turns that the creation and annihilation operators of fermionic discrete lattice models we will be interested in will be expressible in terms of such operators in the framework of a low energy effective field theory.

Given the above definitions, the reason for the name given to the operators $\{\rho(q)\}$ is shown by the following simple manipulations of the expression of the normal-ordered density operator:

$$: \psi^\dagger(x)\psi(x) := \frac{1}{L} \sum_{k,p} e^{i(k-p)x} : c^\dagger_p c_k := \tag{3.17}$$

$$= \frac{1}{L} \sum_{k,q} e^{-iqx} : c^\dagger_{k+q} c_k := \tag{3.18}$$

$$= \frac{1}{L} \sum_k : c^\dagger_k c_k : + \frac{1}{L} \sum_{q \neq 0} e^{-iqx} \sum_k : c^\dagger_{k+q} c_k := \tag{3.19}$$

$$= \frac{N}{L} + \frac{1}{L} \sum_{q \neq 0} e^{-iqx} \rho(q) \tag{3.20}$$

In the last step of the calculation, the normal-ordering sign has been removed due to its redundancy in the case of a product of two fermionic operators labeled by different quantum numbers.

Turning to the discussion of the properties of the density fluctuation operators, it is clear from their definition that they represent a linear combination of operators that create particle-hole excitations . By computing the commutator:

$$[\rho(p), \rho(q)] = \sum_k [c^\dagger_{k+p+q} c_k - c^\dagger_{k+q} c_{k-p}] \tag{3.21}$$

one recognizes that, if $p \neq -q$, the result is trivially shown to be zero by a simple shift in the summation index of the second term, whereas the case $p = -q$ requires more care because it forces us to deal with operators having infinite matrix elements due to the unbounded number of states introduced in our low-energy effective treatment. Indeed, one cannot simply shift the summation index and split the sum in two parts as in the previous case because it would lead to the subtraction of two infinite quantities, which is of course ill-defined.

By introducing the rewriting of the occupation number operator for state k as:

$$c_k^\dagger c_k = \langle c_k^\dagger c_k \rangle_0 + \, : c_k^\dagger c_k : \tag{3.22}$$

where the first term is the vacuum expectation value of the aforesaid operator and the second term represents its normal-ordered version, the commutator can then be rearranged as :

$$[\rho(-q), \rho(q)] = \sum_k [: c_k^\dagger c_k : + \langle c_k^\dagger c_k \rangle_0 - : c_{k+q}^\dagger c_{k+q} : - \langle c_{k+q}^\dagger c_{k+q} \rangle_0] \tag{3.23}$$

The first and third term then cancel each other after splitting the two sums and shifting the summation index, which is now legitimate because the divergencies have been removed by normal-ordering the operators and therefore we are not dealing anymore with the undefined subtraction of two infinities. The second and fourth term instead give the following as a result:

$$[\rho(-q), \rho(q)] = \frac{Lq}{2\pi} \tag{3.24}$$

where the expectation value is taken over the Fermi sea. Finally , the following relation holds:

$$[\rho(p), \rho(q)] = \frac{Lq}{2\pi} \delta_{p,-q} \tag{3.25}$$

By defining :

$$b_q := \sqrt{\frac{2\pi}{Lq}} \, \rho(-q) \tag{3.26}$$

$$b_q^\dagger := \sqrt{\frac{2\pi}{Lq}} \, \rho(q) \tag{3.27}$$

for $q > 0$ only , one recovers the standard bosonic commutation relation:

$$[b_q, b_{q'}^\dagger] = \delta_{q,q'} \tag{3.28}$$

$$[b_q, b_{q'}] = [b_q^\dagger, b_{q'}^\dagger] = 0 \tag{3.29}$$

Remembering relation (3.12), the first consequences of the above definition are the following relations:

$$[b_q, N] = [b_q^\dagger, N] = 0, \;\; \forall q > 0 \tag{3.30}$$

$$b_q |N\rangle_0 = 0, \;\; \forall N \;\; \forall q > 0 \tag{3.31}$$

where the first relation expresses the fact that particle-hole excitations do not change the number of fermions and the second one signals the absence of any particle-hole excitation in the N-particle ground states, which represent the vacuum states for the aforementioned bosonic excitations. Furthermore, it is useful to express the normal-ordered density operator in terms of the bosons as follows:

$$: \psi^\dagger(x)\psi(x) := \frac{N}{L} + \frac{1}{\sqrt{2\pi L}} \sum_{q>0} \sqrt{q} \left[e^{iqx} b_q + e^{-iqx} b_q^\dagger \right] \tag{3.32}$$

As a final remark, the normal-ordering operation is defined as well for bosonic creation and annihilation operators by transposing the b_q's to the right and the $b_q^\dagger$'s to the left without any accompanying sign at each trasposition.

3.3.3 Completeness of the bosonic representation

A crucial theorem due to Haldane (see [16]) ensures the completeness of the bosonic representation of the N-particle Hilbert space H_N, formally expressed by the following condition:

$$\forall |\psi_N\rangle \in H_N \;\; \exists\, f(\{b_q^\dagger\}) \; s.t. \; |\psi_N\rangle = f(\{b_q^\dagger\})|N\rangle_0 \tag{3.33}$$

Such a powerful statement is indeed guaranteeing that the N-particle Hilbert space H_N, which is known to be spanned by the states generated through the action of particle-hole excitations on the corresponding ground state, can be equally spanned by the states resulting from the action of a finite, arbitrary number of b_q^+'s on $|N\rangle_0$, which is of course not obvious at all if one considers the fact that the b_q's represent infinite linear combinations of particle-hole excitations.

3.3.4 Klein factors

The last ingredient one needs to actively perform bosonization is a pair of operators connecting Hilbert spaces with different particle number, which of course cannot be accomplished by the bosonic operators we have just defined in (3.26) and (3.27), since they cannot change the particle number. Such operators are called Klein factors, are denoted by F and $F^\dagger$ and are defined by the properties:

$$[F, b] = [F, b^\dagger] = [F^\dagger, b] = [F^\dagger, b^\dagger] = 0 \tag{3.34}$$

$$F|N\rangle_0 = |N-1\rangle_0 \tag{3.35}$$

$$F^\dagger|N\rangle_0 = |N+1\rangle_0 \tag{3.36}$$

It follows from the definition that F is unitary, i.e. $F^\dagger = F^{-1}$ and that the following commutation rules with the total number operator can be established:

$$[F, N] = F \tag{3.37}$$

$$[F^\dagger, N] = -F^\dagger \tag{3.38}$$

Finally, by acting with the Klein factors on a general N-particle many-body state, which can be always expressed in the form $|\psi\rangle = f(b_q^\dagger)|N\rangle_0$ thanks to (3.33), one obtains:

$$F|\psi\rangle = Ff(\{b_q^\dagger\})|N\rangle_0 = f(\{b_q^\dagger\})F|N\rangle_0 = f(\{b_q^\dagger\})|N-1\rangle_0 \tag{3.39}$$

$$F^\dagger|\psi\rangle = F^\dagger f(\{b_q^\dagger\})|N\rangle_0 = f(\{b_q^\dagger\})F^\dagger|N\rangle_0 = f(\{b_q^\dagger\})|N+1\rangle_0 \tag{3.40}$$

where in the second equality the commutation properties of the Klein factors reported in (3.34) have been used. Such relations are telling us that the action of Klein factors on a general N-particle state generates a new state in which the same set of particle-hole excitations is imposed on the ground state of the Hilbert space space with 1 particle more in the case of $F^\dagger$ and 1 particle less in the case of F.

3.3.5 Useful relations

We are now in a position to give an expression of the fermionic field operator $\psi(x)$ entirely in terms of the number operator, Klein factors and bosonic ladder operators, so that the foundations of the bosonization technique can finally be established and then concretely applied to the study of the systems we will be interested in. The crucial starting observation arises from the computation of the commutator between the bosonic creation and annihilation operators $b_q, b_q^\dagger$ and the fermionic field operator $\psi(x)$, which gives:

$$[b_q, \psi(x)] = -\sqrt{\frac{2\pi}{Lq}}e^{-iqx}\psi(x) \tag{3.41}$$

$$[b_q^\dagger, \psi(x)] = -\sqrt{\frac{2\pi}{Lq}}e^{iqx}\psi(x) \tag{3.42}$$

where the definitions of b_q and $\psi(x)$ in terms of fermionic creation and annihilation operators have been used.

As a consequence, one can argue that:

$$b_q\psi(x)|N\rangle_0 = [b_q, \psi(x)]|N\rangle_0 = \beta_q(x)\psi(x)|N\rangle_0 \tag{3.43}$$

where $\beta_q(x)$ has been introduced as:

$$\beta_q(x) = -\sqrt{\frac{2\pi}{Lq}}e^{-iqx} \tag{3.44}$$

and equation (3.31) has been used. Hence, $\psi(x)|N\rangle_0$ is an eigenstate of the bosonic annihilation operator b_q for every value of $q > 0$ with eigenvalue $\beta_q(x)$. Such states are called coherent states and a detailed calculation presented in [12] shows that their form in terms of Klein factors, bosons and number operator is given by the following equation:

$$\psi(x)|N\rangle_0 = \frac{F}{\sqrt{L}}e^{\frac{i2\pi Nx}{L}}\exp\left(\sum_{q>0}\beta_q(x)b_q^\dagger\right)|N\rangle_0 \tag{3.45}$$

By means of the property (3.33), relation (3.45) can be generalized to an arbitrary N-particle state $|\psi_N\rangle$ as:

$$\psi(x)|\psi_N\rangle = \frac{F}{\sqrt{L}} e^{\frac{i2\pi Nx}{L}} \exp\left(\sum_{q>0} \beta_q(x) b_q^\dagger\right) \exp\left(-\sum_{q>0} \beta_q^*(x) b_q\right) |\psi_N\rangle \quad (3.46)$$

which now acquires the status of an operator identity over the entirety of the Fock space. Equation (3.46), also known as Mattis-Mandelstam formula, lies at the heart of the bosonization prescription.

Let us present a sketch of the proof of the validity of equation (3.46), given its outstanding importance. Since any state $|\psi_N\rangle \in H_N$ can be expressed by means of equation (3.33), then:

$$\psi(x)|\psi_N\rangle = \psi(x) f(\{b_q^\dagger\})|N\rangle_0 \quad (3.47)$$

holds. By exploiting the commutation relation reported in (3.42), one has:

$$\psi(x) f(\{b_q^\dagger\}) = f(\{b_q^\dagger - \alpha_q^*(x)\})\psi(x) \quad (3.48)$$

which in turn can be plugged into equation (3.47) to obtain:

$$\psi(x)|\psi_N\rangle = f(\{b_q^\dagger - \alpha_q^*(x)\})\psi(x)|N\rangle_0 \quad (3.49)$$

Finally, if one rewrites the term $\psi(x)|N\rangle_0$ thanks to (3.45), reorders the resulting terms and exploits the identities:

$$\exp\left(-\sum_{q>0} \beta_q^*(x) b_q\right) f(\{b_q^\dagger\}) \exp\left(\sum_{q>0} \beta_q^*(x) b_q\right) = f(\{b_q^\dagger - \alpha_q^*(x)\}) \quad (3.50)$$

$$\exp\left(\sum_{q>0} \beta_q^*(x) b_q\right) |N\rangle_0 = |N\rangle_0 \quad (3.51)$$

the expression reported in (3.46) is indeed recovered.

Finally, by introducing the bosonic fields:

$$\varphi(x) = -\frac{i}{\sqrt{2\pi}} \sum_{q>0} \beta_q^*(x) e^{-\frac{\beta q}{2}} b_q \quad (3.52)$$

$$\varphi^\dagger(x) = \frac{i}{\sqrt{2\pi}} \sum_{q>0} \beta_q(x) e^{-\frac{\beta q}{2}} b_q^\dagger \quad (3.53)$$

$$\phi(x) = \varphi(x) + \varphi^\dagger(x) \quad (3.54)$$

one can rewrite equation (3.46) in the compact form:

$$\psi(x) = \frac{F}{\sqrt{2\pi\alpha}} e^{\frac{i2\pi Nx}{L}} \exp\left(-i\sqrt{2\pi}\phi(x)\right) \quad (3.55)$$

where the positive real parameter α has the role of a convergence factor which allows to define a proper bosonic theory in 1D. The latter, which did not appear in equation (3.46), is instead needed in equation (3.55) because the expression it contains is not normal-ordered and hence needs to be regularized in order to avoid dealing with unphysical divergencies.

3.4 Bosonization of the XXZ model

3.4.1 Effective field theory for the XXZ model

After having reviewed the most crucial steps toward the definition of a bosonization dictionary that allows to map systematically 1D fermionic systems into auxiliary bosonic ones, we are now going to apply such a technique to the study of the well known 1D spin-$\frac{1}{2}$ XXZ model, defined by the following Hamiltonian:

$$H = J\sum_{j=1}^{M}\left[S_i^x S_{i+1}^x + S_i^y S_{i+1}^y + \Delta S_i^z S_{i+1}^z\right] \tag{3.56}$$

where M denotes the number of sites belonging to the underlying lattice, $J > 0$ is the characteristic energy scale of the system and periodic boundary conditions of the form $\vec{S}_{N+1} \equiv \vec{S}_1$ have been enforced. The spin operators $\{\vec{S}_i\}_{i=1}^{M}$ are defined by the relation:

$$\vec{S}_i = \frac{\hbar}{2}\vec{\sigma}_i \tag{3.57}$$

where $\vec{\sigma}_i = (\sigma_i^x, \sigma_i^y, \sigma_i^z)$ is a three-dimensional vector whose component are given by the celebrated Pauli matrices:

$$\sigma_i^x = \begin{bmatrix} 0 & 1 \\ 1 & 0 \end{bmatrix}_i,\ \sigma_i^y = \begin{bmatrix} 0 & -i \\ i & 0 \end{bmatrix}_i,\ \sigma_i^z = \begin{bmatrix} 1 & 0 \\ 0 & -1 \end{bmatrix}_i \tag{3.58}$$

acting on the local Hilbert space at site i. The commutation relations satisfied by the spin operators are the usual angular momentum commutation relations:

$$\left[S_i^\alpha, S_j^\beta\right] = i\hbar\delta_{ij}\epsilon_{\alpha\beta\gamma}S_i^\gamma \tag{3.59}$$

where it is to be noted that spin operator components at different sites commute between each other and $\epsilon_{\alpha\beta\gamma}$ is the Levi-Civita symbol.

A first noticeable feature of the above Hamiltonian is the fact that it commutes with the total magnetization along the z-axis, i.e.:

$$\left[H, \sum_j S_j^z\right] = 0 \tag{3.60}$$

meaning that such an observable is a good conserved quantum number. Additionally, the XXZ model has been widely studied and is known to exhibit three different phases depending on the values of J and Δ, as displayed in figure (3.4). When $|\Delta| > 1$, then either $\Delta < 0$, resulting in a ferromagnetic ordering in the ground state of the system, or $\Delta > 0$, giving rise instead to antiferromagnetic long-range order. In both these two regions of the phase diagram the low energy excitations are gapped. On the contrary, when $|\Delta| < 1$, then the system is in the so called critical region of the phase diagram, where spin configurations

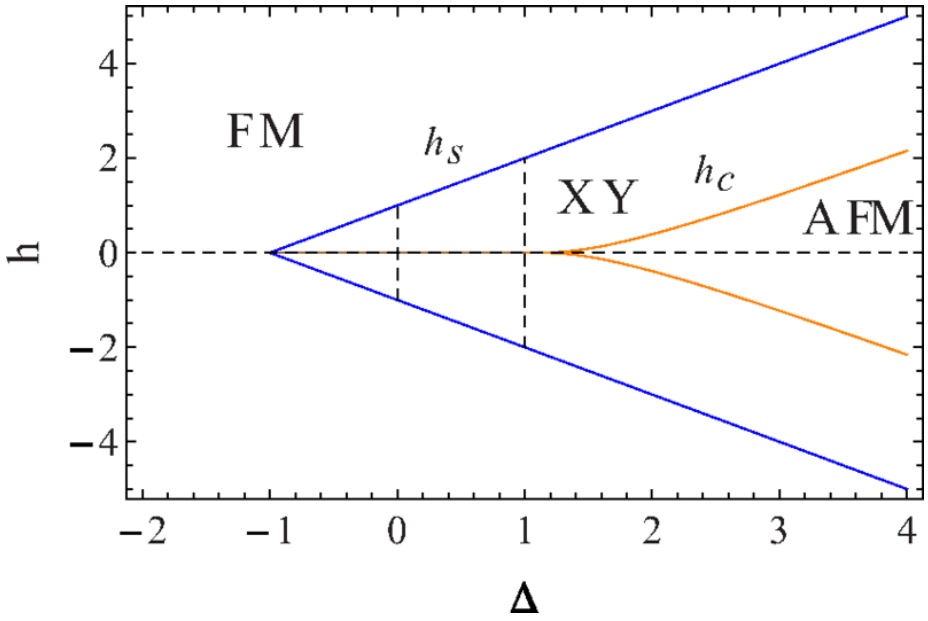

Figure 3.4: Phase diagram of the XXZ model in an external magnetic field h along the z-axis. As far as the purpose of the present work is concerned, our focus will be the line $h = 0$, where, as mentioned in the main text, the segment $|\Delta| < 1$ is associated to the critical, liquid phase, whereas the regions defined by $\Delta < -1$ resp. $\Delta > 1$ host a ferromagnetic resp. antiferromagnetic phase.The image is taken from [32].

along the x-y plane dominate over the ones along the z-axis and the low energy excitations are gapless.

Armed with the purpose of achieving a correct description of the low energy properties of the XXZ spin chain, it is natural to assume that, in the limit of weak interfermion interactions, the only interaction-induced scattering processes which are expected to modify the physics of the system withrespect to the non-interacting point are the ones taking place close to the Fermi points, so that a straightforward weak-coupling bosonization approach can be adopted. In order to make the problem suitable to the bosonization technique, it is useful to map the spin Hamiltonian in (3.56) to a spinless fermion model with the help of the so called Jordan-Wigner transformations, defined through the relations:

$$S_j^z \to c_j^\dagger c_j - \frac{1}{2} \tag{3.61}$$

$$S_j^+ \to c_j^\dagger e^{i\pi \sum_{l=1}^{j-1} c_l^\dagger c_l} \tag{3.62}$$

$$S_j^- \to c_j e^{-i\pi \sum_{l=1}^{j-1} c_l^\dagger c_l} \tag{3.63}$$

where $e^{\pm i\pi \sum_{l=1}^{j-1} c_l^+ c_l}$ represent non-local string operators, whose presence is

strictly necessary to ensure the spin commutation relations to be satisfied by the fermionic representation of the spin operators, and $S_j^+ = S_j^x + iS_j^y$, $S_j^- = (S_j^+)^\dagger$. The key idea behind the clever mapping is the correspondence between the two S_i^z eigenstates $\{|-\frac{1}{2}\rangle_i, |\frac{1}{2}\rangle_i\}$ and the two fermionic Fock space states $\{|0\rangle_i, |1\rangle_i\}$, as follows from (3.61). The naive transformation:

$$S_j^z \to c_j^\dagger c_j - \frac{1}{2} \tag{3.64}$$

$$S_j^+ \to c_j^\dagger \tag{3.65}$$

$$S_j^- \to c_j \tag{3.66}$$

turns out to reproduce the usual spin-$\frac{1}{2}$ commutation relations:

$$\left[S_j^+, S_j^z\right] = -S_j^+ \tag{3.67}$$

$$\left[S_j^-, S_j^z\right] = S_j^- \tag{3.68}$$

$$\left[S_j^+, S_j^-\right] = 2S_j^z \tag{3.69}$$

in the case of a single-site problem. On the other hand, when one tries to directly generalize (3.64), (3.65) and (3.66) to different sites, the mapping is incorrect because, whereas spin operators at different sites commute, fermionic operators anticommute. The cure to such a problem is provided by the aforesaid string operators, whose introduction gives rise to the correct commutation relations:

$$\left[S_j^+, S_l^z\right] = -\delta_{jl} S_j^+ \tag{3.70}$$

$$\left[S_j^-, S_l^z\right] = \delta_{jl} S_j^- \tag{3.71}$$

$$\left[S_j^+, S_l^-\right] = 2\delta_{jl} S_j^z \tag{3.72}$$

By reexpressing the x-component and the y-component of the spin operator $\vec{S}_j$ by their expression in terms of S_j^+ and S_j^- and performing the Jordan-Wigner transformation on the resulting Hamiltonian, the final expression one gets turns out to be:

$$H = -t \sum_{j=1}^{N} [c_j^+ c_{j+1} + h.c.] + V \sum_{j=1}^{N} \left(n_j - \frac{1}{2}\right)\left(n_{j+1} - \frac{1}{2}\right) \tag{3.73}$$

with $n_j = c_j^+ c_j$, $t = \frac{J}{2}$ and $V = J\Delta$ and where the additional minus sign in front of the kinetic term appears as a result of the canonical transformation $c_j \to e^{i\pi j} c_j$, which reveals that the physics of the model is invariant under the replacement $J \to -J$. Thus, the fermionic representation of the model consists of a standard hopping term associated to the kinetic energy contribution and of a nearest-neighbour density-density interaction. Furthermore, as $[H, \sum_j n_j] = 0$, the conserved quantity of the model has now become the total number of particles, related to the z-component of the magnetization through $\sum_j S_j^z = \sum_j n_j - \frac{M}{2}$, where L represents the total number of sites of the lattice structure underlying the 1D system under analysis.

In order to make connection with the bosonization prescription, the lattice fermionic creation and annihilation operators can be manipulated as follows:

$$c_j = \frac{1}{\sqrt{M}} \sum_{k \in BZ} e^{ikj} c_k = \sqrt{a} \frac{1}{\sqrt{Ma}} \sum_{k \in BZ} e^{ikj} c_k \to \tag{3.74}$$

$$\to \sqrt{a} \frac{1}{\sqrt{L}} \sum_{k=-\infty}^{+\infty} e^{ikx} c_k \equiv \sqrt{a}\, \psi(x) \tag{3.75}$$

where a represents the lattice constant, N is the number of lattice sites and the continuum limit $M \gg 1$, $a \ll 1$ such that $Ma = L$ is fixed to the length L of the system has been taken, so that the first Brillouin zone can be extended to an infinite set of discrete values of k over the whole real axis. If one wants to make further progress, the field operator $\psi(x)$ defined above can then be recasted in a more convenient form by performing the following steps:

$$\psi(x) = \frac{1}{\sqrt{L}} \sum_{k=-\infty}^{+\infty} e^{ikx} c_k = \frac{1}{\sqrt{L}} \sum_{k<0} e^{ikx} c_k + \frac{1}{\sqrt{L}} \sum_{k \geq 0} e^{ikx} c_k = \tag{3.76}$$

$$= e^{-ik_F x} \left(\frac{1}{\sqrt{L}} \sum_{k=-\infty}^{k_F} e^{ikx} c_{k-k_F} \right) + e^{ik_F x} \left(\frac{1}{\sqrt{L}} \sum_{k=-k_F}^{+\infty} e^{ikx} c_{k+k_F} \right) \tag{3.77}$$

where a simple shift by $\pm k_F$ in the two summations has been performed, so that $k = 0$ corresponds to the Fermi points.

In the end, by letting $k_F \to +\infty$ in both summation, which amounts to introducing an infinite number of unphysical "positron states" for mathematical convenience while keeping the low energy physics unchanged because of the high energy scales required to excite them, and after performing some clever change of variable, the final result can be summarized as follows:

$$\psi(x) = e^{ik_F x} \psi_R(x) + e^{-ik_F x} \psi_L(x) \tag{3.78}$$

$$\psi_{R,L}(x) = \frac{1}{\sqrt{L}} \sum_{k=-\infty}^{+\infty} e^{\pm ikx} c_k^{R,L} \tag{3.79}$$

where the summation over k runs over the countable set of values $\{k_n = \frac{2\pi n}{L} | n \in \mathbb{N}\}$, two different fermionic branches labeled by the index $\nu \in \{R, L\}$ have been introduced and the corresponding field operators $\psi_{R,L}(x)$, whose long-wavelength Fourier components represent the only physically relevant degrees of freedom in the framework of a low energy approximation, have been defined in (3.79).

Coming back to the problem of formulating an effective bosonic low energy field theory for the XXZ model, it suffices now to plug the expansion (4.2) back into the last expression of (3.75) and expand the various terms appearing in the model Hamiltonian (3.73) to obtain the final result. The kinetic contribution, corresponding to the XX part of the starting spin Hamiltonian, is easily seen to

take the form:

$$H_{kin} = -t\sum_{j=1}^{N}[c_j^\dagger c_{j+1} + h.c.] \approx v_F \int_{-\frac{L}{2}}^{\frac{L}{2}} dx \left[\psi_R^\dagger(x)(-i\partial_x)\psi_R(x) + \psi_L^\dagger(x)(i\partial_x)\psi_L(x)\right] \tag{3.80}$$

having denoted the Fermi velocity as v_F. By employing then the fundamental bosonization relation (3.55), which in the case of two different branches generalizes to:

$$\psi_{R,L}(x) = \frac{F_{R,L}}{\sqrt{2\pi\alpha}} e^{\pm\frac{i2\pi Nx}{L}} \exp\left(-i\sqrt{2\pi}\phi_{R,L}(x)\right) \tag{3.81}$$

the terms of the form $\psi_{R,L}^\dagger(x)(\mp i\partial_x)\psi_{R,L}(x)$ are consequently defined by means of a careful regularization procedure: first one has to normal-order the expressions $\psi_{R,L}^\dagger(x+a)(\mp i\partial_x)\psi_{R,L}(x)$, then expand the result to sub-leading order in a and in the end subtract the divergent constant terms representing the vacuum expectation values of the products of field operators we are attempting to regularize. Finally, by introducing the fields:

$$\phi(x) := \frac{1}{\sqrt{2}}(\phi_L - \phi_R) \tag{3.82}$$

$$\theta(x) := \frac{1}{\sqrt{2}}(\phi_L + \phi_R) \tag{3.83}$$

$$\Pi(x) := \partial_x\theta(x) \tag{3.84}$$

it is possible to express the result as:

$$H_{kin} = \frac{v_F}{2}\int_{-\frac{L}{2}}^{\frac{L}{2}} dx \left[\Pi^2(x) + (\partial_x\phi(x))^2\right] \tag{3.85}$$

$$[\phi(x), \Pi(x')] = i\delta(x - x') \tag{3.86}$$

i.e., the bosonization representation of the kinetic energy contribution amounts to a bosonic quadratic massless field theory associated to the canonically conjugated fields $\phi(x)$ and $\Pi(x)$ and known in 1D many-body quantum physics as Luttinger liquid Hamiltonian.

Moving on to the bosonization of the nearest-neighbour density-density interaction term, it can be shown by means of a trivial computation that it takes the form:

$$H_{int} = V\sum_j n_j n_{j+1} \approx Va\int_{-\frac{L}{2}}^{\frac{L}{2}} dx\,[\rho(x)\rho(x+a) - M(x)M(x+a)] \tag{3.87}$$

where the additional terms arising from the expression of the interaction as reported in (3.73) are neglected since the ground state is assumed to belong to the zero magnetization sector, which is a valid working hypothesis as long as the critical and the antiferromagnetic phase are concerned, and the following

quantities have been introduced:

$$\rho(x) = \psi_R^\dagger(x)\psi_R(x) + \psi_L^\dagger(x)\psi_L(x) \tag{3.88}$$

$$M(x) = \psi_R^\dagger(x)\psi_L(x) + \psi_L^\dagger(x)\psi_R(x) \tag{3.89}$$

As the formulas defining the fields $\rho(x)$ and $M(x)$ clarify, the former introduces low energy intrabranch scattering processes in the interaction Hamiltonian (3.87), whereas the latter gives rise to interbranch scattering events around the Fermi points, where the involved electrons change their wave vector by an amount $\pm 2k_F$. By expressing the fermionic fields in terms of the bosonic ones, the final result turns out to be:

$$H_{int} \approx \frac{2Va}{\pi} \int_{-\frac{L}{2}}^{\frac{L}{2}} dx \left(\partial_x \phi(x)\right)^2 - \frac{2Va}{(2\pi\alpha)^2} \int_{-\frac{L}{2}}^{\frac{L}{2}} dx \cos\left[4\sqrt{\pi}\phi(x)\right] \tag{3.90}$$

In the end, collecting all terms together and properly rescaling the fields through a canonical transformation, the final expression for the bosonized version of the model Hamiltonian takes the form:

$$H = H_0 + H_{int} = \frac{u}{2} \int_{-\frac{L}{2}}^{\frac{L}{2}} dx \left[\pi K \Pi^2(x) + \frac{1}{\pi K} \left(\partial_x \phi(x)\right)^2\right] - g \int_{-\frac{L}{2}}^{\frac{L}{2}} dx \cos\left[4\phi(x)\right] \tag{3.91}$$

where $g = \frac{2Va}{(2\pi\alpha)^2}$ and an effective velocity v and a dimensionless parameter K, also known as Luttinger parameter, have been defined as:

$$u = v_F \sqrt{1 + \frac{4Va}{\pi v_F}} \tag{3.92}$$

$$K = \frac{1}{\sqrt{1 + \frac{4Va}{\pi v_F}}} \tag{3.93}$$

Hence, the XXZ model in the zero magnetization sector turns out to be described by the celebrated sine-Gordon model in bosonization language. Before presenting any rigorous result, it is quite clear on an intuitive level that, while the quadratic terms of the Hamiltonian enhance fluctuations of the field $\phi(x)$, the cosine term will instead promote its ordering by locking it into one of the maxima of the cosine, resulting in a competition between the two aforementioned terms. Formally, the standard approach one employs to tackle the study of the criticality of the model relies on the application of renormalization group (RG) techniques to the action deriving from (3.91). In particular, a first order perturbative RG calculation shows the validity of the following RG flow equation for the coupling constant g:

$$\frac{dg(l)}{dl} = \left(2 - 4K(l)\right) g(l) \tag{3.94}$$

Hence, even the first order result for the renormalization of the coupling g captures the most crucial feature of the critical behaviour of the model.

As a matter of fact, when $K > K_c = \frac{1}{2}$, which is verified as long as the interaction strength V is not too large, as shown by the perturbative expression (3.93) for the Luttinger parameter found by means of the bosonization technique, the parameter g is driven towards a zero value by the RG flow, certifying the irrelevance of the cosine term in such a regime: the phase described in this region of the phase diagram is the critical one, in which kinetic fluctuations dominate over the charge ordering effects induced by the interaction. A more complicated second order RG computation (see, e.g., [1]) shows that in this case the low energy, long wavelength physics is governed by a purely quadratic Hamiltonian with a renormalized Luttinger parameter K^* whose value depends on the values of K and g in the original model Hamiltonian.

Thus, the resulting correlation functions, which can be computed exactly thanks to the quadratic form of the action corresponding to the Luttinger liquid Hamiltonian, display a power law decay governed by exponents exhibiting a non-universal dependence on the microscopic interactions, establishing a form of quasi-long-range order in the system. As an example, the following expressions of spin correlators are reported:

$$\langle S^z(x)S^z(0)\rangle = \frac{C_1}{x^2} + C_2\frac{\cos(2k_F x)}{x^{2K}} \tag{3.95}$$

$$\langle S^+(x)S^-(0)\rangle = C_3\left(\frac{1}{x}\right)^{2K+\frac{1}{2K}} + C_4\frac{\cos(2k_F x)}{x^{2K}} \tag{3.96}$$

where the multiplicative factors C_i are non-universal amplitudes and $x = ja$ is the value of the spatial coordinate on the underlying lattice. The derivation of the expression of the spin correlators proceeds by expressing the spin operators in terms of the fermionic lattice operators thanks to the Jordan-Wigner transformations. These are then rewritten as functions of the bosonic fields through the bosonization prescription, so that the aforesaid correlators can be computed with the help of standard path integral techniques as averages of functions of bosonic fields over a quadratic bosonic Hamiltonian. The S_i^z operator, being nothing but the normal-ordered density, takes the form:

$$S_j^z = n_j - \frac{1}{2} \approx \frac{1}{\pi}\partial_x\phi(x) + \frac{(-1)^{\frac{x}{a}}}{\pi\alpha}\cos\left[2\phi(x)\right] \tag{3.97}$$

whereas the term in the exponent of the string operator can be manipulated as follows:

$$\sum_j c_j^\dagger c_j \approx \int_{-\frac{L}{2}}^{x} dy\left[\frac{1}{2a} + \psi_R^\dagger(y)\psi_R(y) + \psi_L^\dagger(y)\psi_L(y) + e^{-i2k_F y}\psi_R^\dagger(y)\psi_L(y) + h.c.\right] \approx \tag{3.98}$$

$$\approx \int_{-\frac{L}{2}}^{x} dy\left[\frac{1}{2a} + \rho(x)\right] = \frac{x}{2a} + \frac{1}{\pi}\phi(x) + const. \tag{3.99}$$

where the oscillating factors have been dropped out after the first (approximate) equality and the constant contribution is to be regarded as a boundary effect

which disappears in the thermodynamic limit. Thus, the string operator is wonderfully local in bosonization language and, by plugging its expression into (3.62) and (3.63), one obtains (see [1] for details):

$$S^+(x) \propto e^{-i\theta(x)}\{(-1)^{\frac{x}{a}} + \cos[2\phi(x)]\} \tag{3.100}$$

Turning our attention back to the physical implications of the Luttinger liquid Hamiltonian, it is worth noticing that the $S^z - S^z$ correlation function contains both a $q \sim 0$ Fourier component, characterizing nearly ferromagnetic correlations, and a $q \sim 2k_F$ term, describing the nearly antiferromagnetic ones: in the case $K > 1$, corresponding to the presence of attractive interactions between the fermions or, equivalently, to ferromagnetic interactions in the spin chain formulation, the antiferromagnetic correlations are suppressed with respect to the ferromagnetic ones, whereas the opposite scenario is realized in the case $K < 1$, which is instead associated to repulsive fermion-fermion interactions or antiferromagnetic spin-spin coupling. The results are confirmed by the outcome of the numerical simulations carried out by means of the density matrix renormalization group (DMRG) algorithm in the liquid phase, as shown in the section dedicated to the numerical characterization of the phase diagram of the model. As a final remark concerning the critical, quasi-long-range ordered phase, it is worth mentioning that the corresponding low energy excitations, described by density fluctuation modes whose collective nature is consistent with the expectation that the enhancement of fluctuations in reduced dimensionality enforces the replacement of the single-particle picture of excitations valid in higher-dimensional systems with a multiparticle one, exhibit a gapless spectrum.

Instead, when $K < K_c = \frac{1}{2}$, which occurs when the interaction parameter V exceeds a critical value V_c, the coupling constant g flows to infinity, meaning that the cosine term is relevant: the phase described in this case corresponds to a Mott insulator, defined as an insulating state driven by electron-electron interactions whose density profile shows a periodic modulation arising from the particle localization on the lattice sites, which is the most convenient configuration from the energetic point of view in order to minimize repulsion. The Mott insulator is in turn described in a field theoretical treatment by the locking of the field $\phi(x)$ into one of the values $\phi_n = 0 + \frac{\pi n}{2}$, chosen in such a way to minimize the dominant interaction term in the sine-Gordon Hamiltonian.

A first striking consequence of the aforementioned ordering is the opening of a gap in the excitation spectrum, as a straightforward derivation of the Hamiltonian governing the behaviour of the small oscillations of the field $\delta\phi(x)$ around the ordered configuration $\phi(x) = 0$ shows. Indeed, by writing $\phi(x) = 0 + \delta\phi(x)$ and expanding up to second order the resulting cosine term, the Hamiltonian takes the form:

$$H[\delta\phi(x)] = H_0[\delta\phi(x)] + 8g \int_{-\frac{L}{2}}^{\frac{L}{2}} dx\, \delta\phi^2(x) \tag{3.101}$$

where H_0 denotes the standard quadratic Luttinger liquid Hamiltonian. Hence, even at the level of a straightforward analysis of the strong coupling limit, one

captures the emergence of a mass term associated to the aforesaid excitations, which results in the finite energy cost required to excite them. In conjunction to the gapped nature of the charge ordered state, the correlation functions turn into exponentially decaying functions, whose decay takes place over a characteristic length scale, widely known as correlation length in the statistical physics language, which, contrarily to what happens in the Luttinger liquid phase, is finite in the Mott insulating state and inversely proportional to the mass coefficient in a strong coupling regime.

As a final concluding remark, one can observe that there exist also different kind of low energy excitations, called solitons, that take the field ϕ from one of the prescribed ordering values to another one and can form non trivial bound states between each other, exhibiting a rich and fascinating physics. We will not anyway dwell on their properties any further in the remainder of the text. The whole contents of the physics of the Mott insulator is again recovered by a numerical treatment of the system in the gapped phase by means of DMRG simulations, as will be discussed in the next section.

3.5 Numerical results

The numerical characterization of the XXZ model has been carried out by performing DMRG simulations with the help of the ITensor C++ library (see [17]) on the fermionic formulation of the original lattice Hamiltonian for lattice sizes comprised between $L = 61$ and $L = 111$ sites and in presence of open boundary conditions, those being the ones which maximize the efficiency of the DMRG algorithm. As a technical remark, it is worth mentioning that the DMRG simulations on the fermionic formulation of the XXZ model involve the proper tuning of two simulation parameters, namely the number of of lattice sites and the associated filling of the system, in order to satisfy precise commensurability conditions of the underlying lattice to the charge density wave configuration appearing in the gapped phase and whose unit cell is represented as ($\bullet\circ$), where the black dot represents an occupied site and the white dot is associated to an empty one. Indeed, due to the tendency of particles on a finite lattice to stick to the boundary sites in order to minimize the repulsive interaction contribution to the energy of the ground state configuration, it is easy to realize that the only way to accomodate the aforementioned crystalline configuration on a finite lattice while placing a pair of particles on the right resp. left boundary site consists in choosing the number of lattice sites as $L_p = 2p + 1$ and the corresponding filling as $N_p = p + 1$, where p is a non-negative integer.

As far as the characterization of the Luttinger liquid phase is concerned, the values of the model parameters have been chosen to be $t = 1, V = 0.5$, thus satisfying $J = 2$ and $\Delta = \frac{V}{J} = 0.25 < \Delta_c = 1$ in terms of the spin model parameters, so that the exploration of the physics of the critical phase is made possible. As shown in figure (**??**), the absence of long range order for values of the anisotropy parameter satisfying $|\Delta| < 1$ is witnessed by a density profile which closely resembles the uniform average site occupation characteristic of

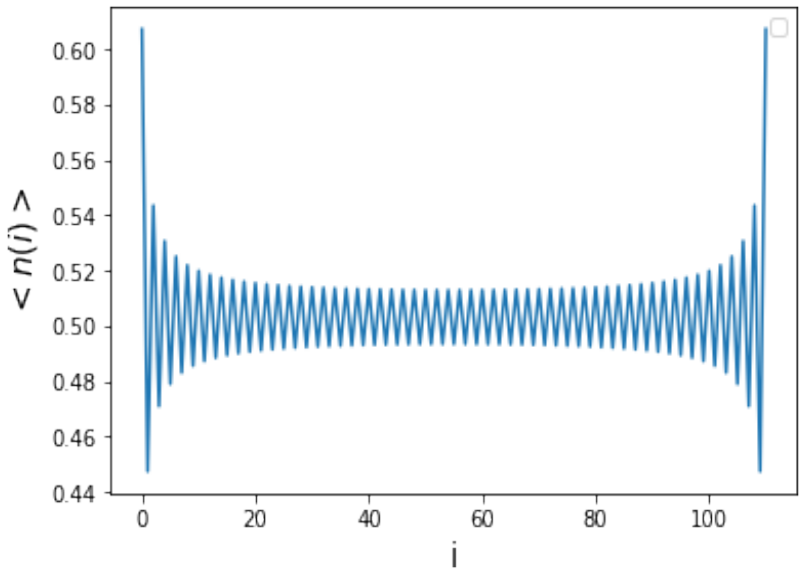

Figure 3.5: Fermionic density profile for $J = 2, \Delta = 0.25$ on a lattice of $L = 111$ sites.

the Luttinger liquid phase, as will be formally proven in the next chapter. The presence of small oscillations around the 0.5 filling and the enhancement of the density at the edges of the lattice for energy minimization purposes are due to unavoidable finite-size effects whose manifestation can be attenuated in the bulk by increasing the system size. Additionally, by recalling (3.61), it is trivial to see that a uniform density in the fermionic model corresponds to the average magnetization being equal to zero, which in turn agrees with the intuitive idea that small values of Δ make the exchange interaction along the z-axis negligible with respect to the couplings along the x-axis and the y-axis, thus leading to the absence of long-range order in the magnetization profile along the z-axis.

A further reassuring result is presented in figure (3.6), where the density-density correlation function ($S^z - S^z$ correlation function in the spin language) of the XXZ model in the critical phase is seen to display the characteristic power law decay predicted in the framework of Luttinger liquid theory, whose results can be directly compared to the numerical ones in order to test the agreement between the two approaches to tackle the study of the system. In particular, a trivial curve fitting procedure of the spin correlations to the bosonization prediction (3.95) allows to extract numerically the value of the Luttinger parameter, which is in turn compared to the perturbative expression (3.93) obtained by means of bosonization, showing thereby an agreement up to discrepancies of the order of at most 5%.

As a concluding remark with regard to the characterization of the Luttinger

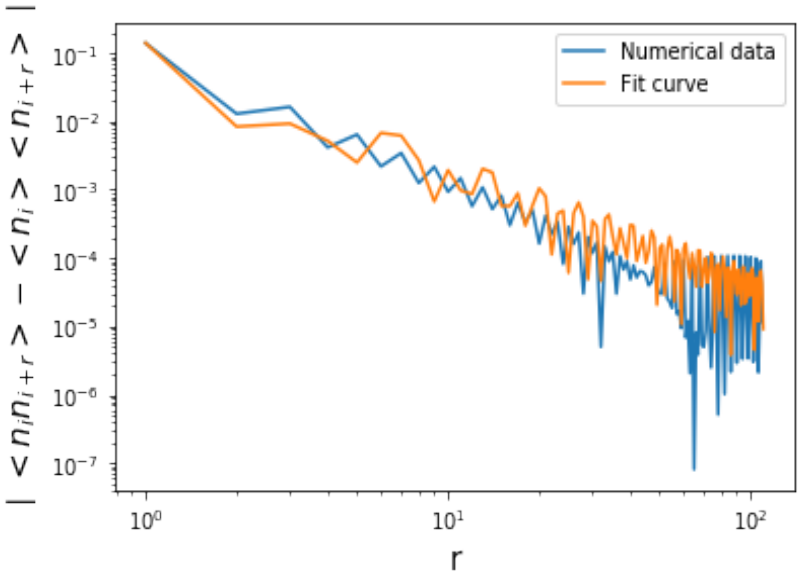

Figure 3.6: Density-density correlation function for $J = 2, \Delta = 0.25$ on a lattice of $L = 111$ sites. The fitting of the numerical data to the field-theoretical result gives an estimate $K_{est} \approx 0.803$, hence showing an excellent agreement with the analytical prediction $K \approx 0.782$ given by (3.93).

liquid phase, the gapless nature of its excitation spectrum has been investigated by examining the finite-size scaling of the so called energy gap the single-particle excitation spectrum, defined by the relation:

$$G(N, L) = E(N + 1, L) + E(N - 1, L) - 2E(N, L) \tag{3.102}$$

where $E(N, L)$ indicates the ground state energy of the system in presence of N particles on a lattice of size L. Indeed, as indicated in figure (3.7), the latter quantity has been computed in half-filling conditions for lattice sizes ranging from $L = 61$ to $L = 111$, so that its value in the infinite-size limit could be estimated by fitting the data points to a power law of the form:

$$f(L; G_\infty, A, m) = G_\infty + \frac{A}{L^m} \tag{3.103}$$

where G_∞, A, m are the fitting parameter and the aforesaid estimate of the energy gap in the single-particle excitation spectrum is given by G_∞. The obtained value turns out to be of order 10^{-3}, which, given the presence of finite-size effects and the limited number of data points available for the fitting procedure, is in perfect agreement with the absence of a gap in the Luttinger liquid phase.

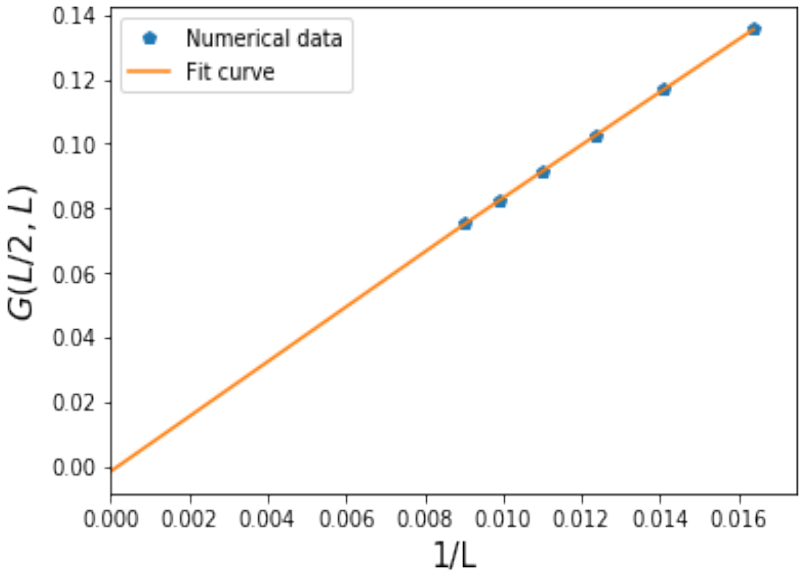

Figure 3.7: Finite-size scaling of the energy gap in the single-particle excitation spectrum for $J = 2, \Delta = 0.25$ for lattice sizes ranging from $L = 61$ to $L = 111$ sites.

On the other hand, the outcomes of the DMRG simulations confirm the emergence of a pronounced charge-density wave order in the case $t = 1$ and $V = 4$, corresponding in turn to an evident antiferromagnetic ordering of the z-component of the lattice spins when the model parameters are set to $J = 2$ and $\Delta = \frac{V}{J} = 2 > \Delta_c = 1$. In fact, the density profile presented in figure (3.8) can be thought of as being generated by the periodic repetition in space of the primitive unit cell ($\bullet\circ$). The resulting picture of the system is a Mott insulating state, where the fermions are strongly localized on a specific pattern of sites in a way that they give rise to a crystalline configuration. Once again, thanks to (3.61) it is possible to reinterpret the result obtained in the fermionic setting with reference to the spin system, where the z-axis magnetization will exhibit the long-range staggered behaviour which identifies an antiferromagnetic-like ordering.

Furthermore, as expected, the finite-size scaling of the energy gap in the single-particle excitation spectrum exhibited in figure (3.9) shows, by means of the very same fitting procedure as the one employed in the case of the characterization of the point in the Luttinger liquid phase, a value $G_\infty \approx 1.465$ of the same order of the sampled finite-size values and manifestly larger than zero, thereby strongly suggesting that the numerical data are in good agreement with the field-theoretical prediction of the opening of a finite gap in the low energy excitation spectrum.

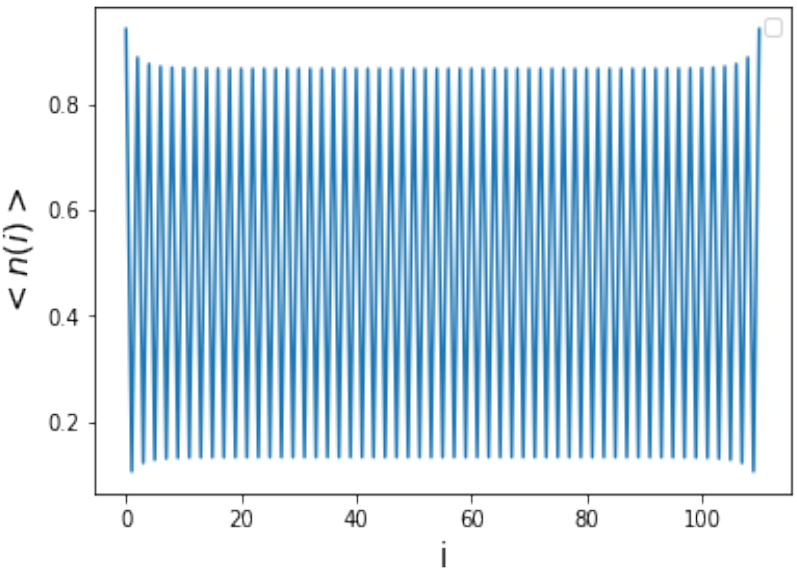

Figure 3.8: Fermionic density profile for $J = 2, \Delta = 2$ on a lattice of $L = 111$ sites.

The statement concerning the appearence of a finite correlation length is reported as well in numerical results such as the one shown in figure (**??**), where the exponential behaviour which identifies the behaviour of the correlation functions in the gapped Mott insulating state can be observed directly. In particular, fitting the numerically obtained profile of the density-density correlator as a function of the distance to an exponential curve of the generic form:

$$f(x; A, b, l) = Ae^{-\left(\frac{x}{l}\right)^b} \tag{3.104}$$

where A, b, l are fitting parameters, demonstrates the exponential decay of the aforementioned quantity.

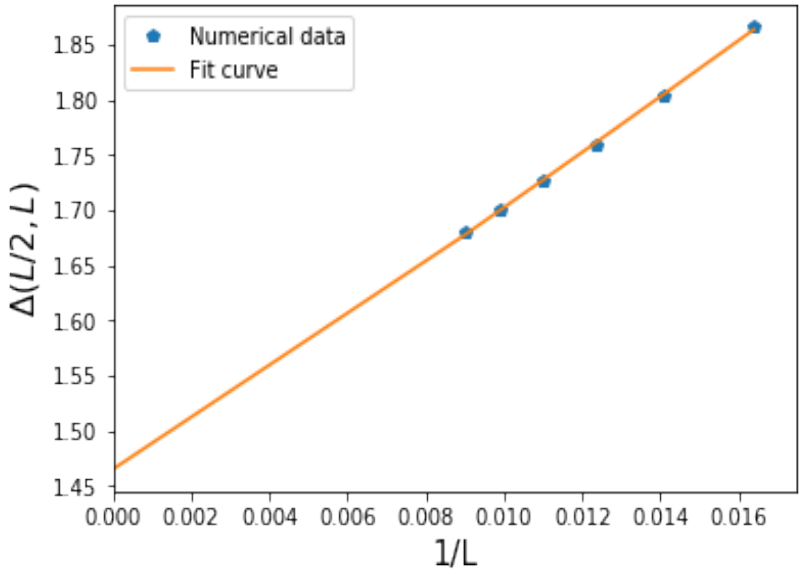

h

Figure 3.9: Finite-size scaling of the energy gap in the single-particle excitation spectrum for $J = 2, \Delta = 2$ for lattice sizes ranging from $L = 61$ to $L = 111$ sites.

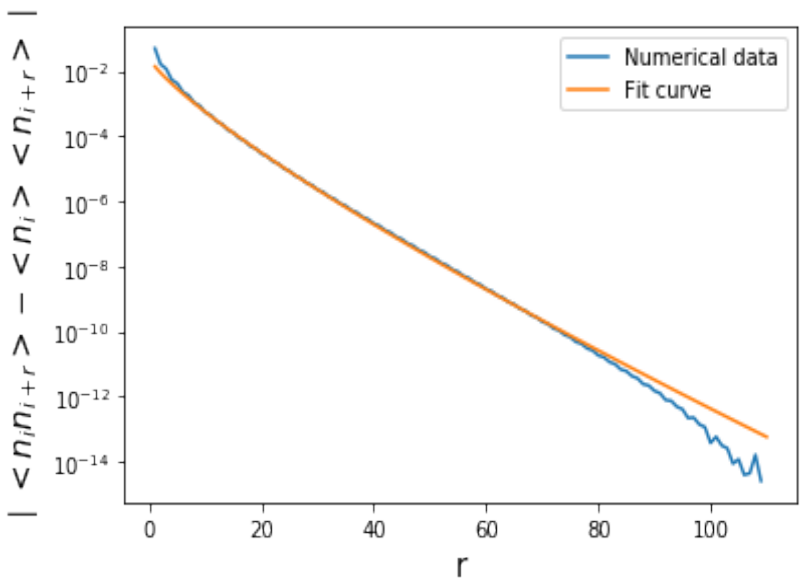

Figure 3.10: Density-density correlation function for $J = 2, \Delta = 2$ on a lattice of $L = 111$ sites..

Chapter 4

$t - U_1 - U_2$ model at half-filling

4.1 Introduction

The goal of the present chapter is the recharacterization of the zero-temperature phase diagram of the $t - U_1 - U_2$ model in half-filling conditions. The model Hamiltonian we are going to refer throughout the exposition is reported here for reference purposes:

$$H = -t \sum_i \left[c_i^\dagger c_{i+1} + h.c. \right] + U_1 \sum_i n_i n_{i+1} + U_2 \sum_i n_i n_{i+2} \tag{4.1}$$

The analysis proceeds both on analytical and numerical grounds: a low energy effective field theory will be derived by making use of the bosonization technique and its results will be confirmed and complemented by the outcomes of the numerical simulation.

4.2 Phase diagram characterization

The starting point of our analysis will be the bosonization of the Hamiltonian of the model, whose only difference with respect to the fermionic version of the XXZ model lies in the presence of the long-range interaction term represented by the next-to-nearest-neighbour density-density term. Hence, let us try to write its bosonized expression and then add it to the result obtained for the XXZ model at half-filling or, equivalently, in the zero magnetization sector of the corresponding spin model.

In a weak-coupling bosonization approach, the fermionic lattice operator is expanded around the two Fermi points of the spectrum of the non-interacting system in terms of the slowly varying field operators $\psi_R(x)$ and $\psi_L(x)$ as:

$$c_j \approx \sqrt{a} \left[e^{ik_F x} \psi_R(x) + e^{-ik_F x} \psi_L(x) \right] |_{x=ja} \tag{4.2}$$

having denoted the lattice spacing as a and the Fermi wavevector as k_F.

The expansion in (4.2) is then plugged into the long-range density-density interaction term $U_2 \sum_j n_j n_{j+2} = U_2 \sum_j c_j^\dagger c_j c_{j+2}^\dagger c_{j+2}$ to give:

$$U_2 \sum_j n_j n_{j+2} \approx \tag{4.3}$$

$$U_2 a^2 \sum_j \left[\rho(x) + e^{-i2k_F x}\psi_R^\dagger(x)\psi_L(x) + e^{i2k_F x}\psi_L^\dagger(x)\psi_R(x)\right] \times \tag{4.4}$$

$$\times \left[\rho(x+2a) + +e^{-i2k_F x}\psi_R^\dagger(x+2a)\psi_L(x+2a) + e^{i2k_F x}\psi_L^\dagger(x+2a)\psi_R(x+2a)\right] |_{x=ja} \tag{4.5}$$

where we have introduced the field $\rho(x)$ as:

$$\rho(x) = \psi_R^\dagger(x)\psi_R(x) + \psi_L^\dagger(x)\psi_L(x) \tag{4.6}$$

While the former induces intrabranch scattering events, the subsequent terms in (4.3) are associated to interbranch processes.

Multiplying all terms together and neglecting the ones containing rapidly oscillating terms on a length scale of the order of the lattice spacing, one gets to the expression:

$$U_2 \sum_j n_j n_{j+2} \approx U_2 a \int_{-\frac{L}{2}}^{\frac{L}{2}} dx \left[\rho(x)\rho(x+2a) + M(x)M(x+2a)\right] \tag{4.7}$$

having set:

$$M(x) = \psi_R^\dagger(x)\psi_L(x) + \psi_L^\dagger(x)\psi_R(x) \tag{4.8}$$

It is worth mentioning that, in order to write down a proper bosonized version of the interaction term, it is important to bear in mind while performing the calculations leading to the expression in (4.7) that, since we are working at half-filling ($k_F = \frac{\pi}{2a}$), the following relations hold:

$$e^{\pm i2k_F a} = -1 \tag{4.9}$$

$$e^{\pm i4k_F x}|_{x=ja} = 1 \tag{4.10}$$

Hence, while multiplying all terms arising from the expression of the interaction contribution we are trying to bosonize, it is crucial to be careful not to neglect the ones containing the complex exponential in (4.10) as a factor.

The final step of the recipe requires the application of the Mattis-Mandelstam formula, which allows for the representation of the Hamiltonian of the theory in terms of bosonic continuous degrees of freedom. By plugging the relation:

$$\psi_{R,L}(x) = \frac{F_{R,L}}{\sqrt{2\pi\alpha}} e^{\pm i \frac{2\pi N_{R,L}}{L} x} e^{-i\sqrt{2\pi}\phi_{R,L}(x)} \tag{4.11}$$

into (4.7) and working without loss of generality in the subspace $N_R = N_L = 0$, the terms in the continuum limit of the lattice long-range interaction give respectively:

$$\rho(x)\rho(x+2a) \approx \frac{1}{\pi}\left(\partial_x\phi(x)\right)^2 \tag{4.12}$$

$$M(x)M(x+2a) \approx \frac{1}{2(\pi\alpha)^2}\cos\left[4\sqrt{\pi}\phi(x)\right] - \frac{4}{\pi}\left(\partial_x\phi(x)\right)^2 \tag{4.13}$$

where constant, though divergent, terms arising from the introduction of an infinite number of states in the field-theoretical treatment have been discarded due to their unphysical origin and the field $\phi(x)$ has been defined as:

$$\phi(x) = \frac{1}{\sqrt{2}}\left(\phi_L(x) - \phi_R(x)\right) \tag{4.14}$$

Inserting the obtained expressions in (4.7), the long-range interaction contribution to the bosonized version of the model Hamiltonian reads:

$$U_2\sum_j n_j n_{j+2} \approx \frac{U_2}{2\pi^2 a}\int_{-\frac{L}{2}}^{\frac{L}{2}} dx\cos\left[4\sqrt{\pi}\phi(x)\right] - \frac{3U_2 a}{\pi}\int_{-\frac{L}{2}}^{\frac{L}{2}} dx\left(\partial_x\phi(x)\right)^2 \tag{4.15}$$

where the inverse cutoff in momentum space has been replaced on physical grounds by the lattice spacing a. By adding it to the result previously obtained for the XXZ model, the final expression of the Hamiltonian defining the effective bosonic theory for the $t - U_1 - U_2$ model takes the form:

$$H = \frac{u}{2}\int_{-\frac{L}{2}}^{\frac{L}{2}} dx\left[\pi K\Pi^2(x) + \frac{1}{\pi K}\left(\partial_x\phi(x)\right)^2\right] + g\int_{-\frac{L}{2}}^{\frac{L}{2}} dx\cos\left[4\phi(x)\right] \tag{4.16}$$

where the reader is referred to the chapter dedicated to the review of the bosonization technique for the definition of the conjugate momentum field $\Pi(x)$.

The value of the phenomenological parameters u and K attached to the quadratic massless part of the bosonized Hamiltonian take in the present case the following form as a function of the microscopic interaction parameters:

$$u = v_F\sqrt{1 + \frac{2a}{\pi v_F}\left(2U_1 - 3U_2\right)} \tag{4.17}$$

$$K = \frac{1}{\sqrt{1 + \frac{2a}{\pi v_F}\left(2U_1 - 3U_2\right)}} \tag{4.18}$$

having indicated the Fermi velocity as v_F. The expressions (4.17) and (4.18) are of course reliable only in the perturbative limit $U_1, U_2 \ll 1$. On the other hand, the coefficient in front of the cosine interaction term reads:

$$g = \frac{U_2 - U_1}{2\pi^2 a} \tag{4.19}$$

making it evident that the two microscopic interaction mechanisms are competing against each other.

4.2.1 Luttinger liquid phase

Let us now turn our discussion towards the physical implications of the Hamiltonian (4.16). Of course, when both U_1 and U_2 are negligibly small, the Luttinger parameter has a value which is larger than $K_c = \frac{1}{2}$ and the cosine term turns out to be irrelevant in the low energy limit. Such a regime describes the standard Luttinger liquid phase adiabatically connected with the non-interacting point.

The aforementioned phase exhibits quasi-long-range-order, defined by the scale-free power law decay of the correlators. The associated exponents are highly non-universal functions of the microscopic interaction parameters through the Luttinger parameter K. As an example, the behaviour of the density-density correlation function is reported:

$$\langle \rho(x+r)\rho(x)\rangle = \frac{C_1}{r^2} + C_2 \frac{\cos(2k_F r)}{r^{2K}} \tag{4.20}$$

where C_1 and C_2 are non-universal amplitudes which do not affect the large distance behaviour of the density-density correlation function.

At the same time, the system does not exhibit a spontaneous breaking of the discrete translational symmetry, typical instead of the charge-ordered phases, as the subsequent cumbersome calculation shows. Quantitative informations concerning the density profile of the system can be obtained in the framework of the bosonization recipe by computing the ground state expectation value $\langle n_j \rangle$ as:

$$\langle n_j \rangle - \frac{1}{2} \propto \langle \rho(x) + e^{-i2k_F x}\psi_R^\dagger(x)\psi_L(x) + e^{i2k_F x}\psi_L^\dagger(x)\psi_R(x)\rangle = \tag{4.21}$$

$$= \left\langle \frac{\partial_x \phi(x)}{\pi} + \frac{(-1)^{\frac{x}{a}}}{\pi a}\cos\left[2\phi(x)\right] \right\rangle \tag{4.22}$$

Since the field configuration weights are generated according to a quadratic action, the various averages can be computed by carefully exploiting Wick's theorem. The derivative term gives trivially a zero contribution to the average, since, as established by the aforementioned Wick's theorem, averages of products of an odd number of gaussian fields are equal to zero. The average of the cosine term requires instead, contrarily to the preceding contribution, more care and a deeper treatment.

Let us consider:

$$\langle \cos\left[2\phi(x)\right]\rangle = \sum_{n=0}^{+\infty} \frac{(-4)^n}{(2n)!}\langle \phi^{2n}(x)\rangle \tag{4.23}$$

where the Taylor expansion of the cosine function has been written down. Wick's theorem prescription for the $2n-$th power of the field $\phi(x)$ demands:

$$\langle \phi^{2n}(x)\rangle = \frac{(2n)!}{2^n n!}\langle \phi^2(x)\rangle^n \tag{4.24}$$

where the $n-$dependent factor in front of the $n-$th power of the average of the square of the field accounts for the multiplicity associated to the number of ways

in which the $2n$ field factors in the product we have to average can be regrouped in distinct pairs. By plugging the result (4.24) in (4.23), the expression takes finally the form:

$$\langle \cos\left[2\phi(x)\right]\rangle = \sum_{n=0}^{+\infty} \frac{\left[-2\langle\phi^2(x)\rangle\right]^n}{n!} = e^{-2\langle\phi^2(x)\rangle} \tag{4.25}$$

Thus, the problem has reduced to the computation of the expectation value $\langle\phi^2(x)\rangle$, which is known to be the zero value of the correlator G of the field theory, defined through the relation:

$$G(x-y) = \langle\phi(x)\phi(y)\rangle \tag{4.26}$$

In the framework of a quadratic massless action in $1+1$ dimension, as it is the case for our problem, it is a textbook exercise to show that it only depends logarithmically on the distance $r = ||x-y||$, as opposed to what occurs in higher spatial dimensions, where it exhibits a power law decay as a function of the separation between the two points where the fields are evaluated. In symbols:

$$G(x-y) = C_0 - \frac{K}{4}\log r \tag{4.27}$$

where C_0 is an irrelevant constant and the result rigorously holds in the infinite size, zero temperature limit.

Turning our attention back to the determination of the density profile in the Luttinger liquid phase, the average of the cosine term can be rewritten in the end as:

$$\langle \cos\left[2\phi(x)\right]\rangle = \lim_{r\to 0^+} e^{-2G(r)} = 0 \tag{4.28}$$

by making use of the behaviour reported in (4.27). Hence, the expected value of the density fluctuations on top of the homogeneous profile of the half-filled system is identically zero, consistently with the behaviour expected for a quasi-long-range-ordered liquid phase.

As fas as the numerical characterization of the Luttinger liquid phase is concerned, the most interesting results have been obtained, inspired by [2], by performing DMRG simulations at the point $U_1 = 4, U_2 = 2$ of the phase diagram in presence of open boundary conditions and for lattice sizes ranging from $L = 38$ to $L = 110$. The density profile, shown in figure (4.1), seems to support the analytical prediction: indeed, despite the strong finite-size effects arising from the relatively small lattices we have considered, one can argue that the thermodynamic limit is reproduced in the bulk of the system, where the density oscillations are strongly suppressed and a perfectly homogeneous configuration is observed.

The power law behaviour of the correlation functions is equally well evidentiated in the outcome of the aforesaid simulations. In particular, the single-particle correlation function $\langle c_i^\dagger c_{i+r}\rangle$, the pairing correlation function $\langle c_i^\dagger c_{i+1}^\dagger c_{i+r} c_{i+r+1}\rangle$ and the density-density correlation function $\langle n_i n_{i+r}\rangle - \langle n_i\rangle\langle n_{i+r}\rangle$ have been

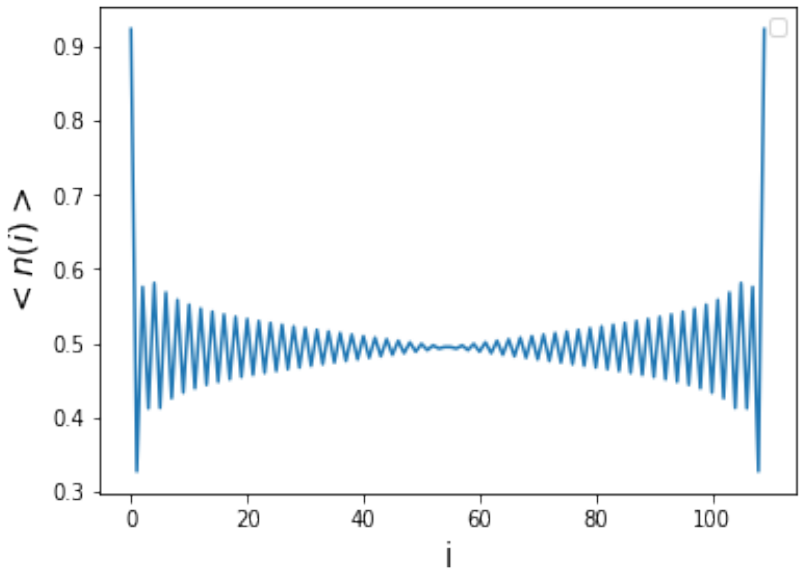

Figure 4.1: Fermionic density profile exhibited by the system for $U_1 = 4, U_2 = 2$ on a lattice of $L = 110$ sites.

measured by the DMRG simulation, giving reassuring results. As a reference, the behaviour of the single-particle correlation function is reported as a function of the distance in figure (4.2), where the power law functional form is further supported by a trivial curve fitting procedure of a function of the form reported below to the numerical data:

$$f(x; A, b, C, \omega, e) = \frac{A}{x^b} + C\frac{\cos(\omega x)}{x^e} \tag{4.29}$$

where A, b, C, ω, e are fitting parameters.

An additional information made available by the numerical outcomes obtained by analysing the aforesaid phase diagram point belonging to the Luttinger liquid phase region concerns the absence of a gap in the single-particle excitation spectrum in the thermodynamic limit. The latter is defined as:

$$\Delta(N, L) = E(N + 1, L) + E(N - 1, L) - 2E(N, L) \tag{4.30}$$

where $E(N, L)$ represents the ground state energy of the system with L lattice sites and N fermionic particles. The aforesaid quantity has been computed for lattice sizes ranging from $L = 38$ to $L = 110$ sites, so that its finite-size scaling has been determined with the goal of extrapolating its value in the infinite size limit. The resulting data points are fitted to a first order polynomial in the inverse system size, expressed in symbols as:

$$\Delta_{fit}(L; \Delta_\infty, A) = \Delta_\infty + \frac{A}{L} \tag{4.31}$$

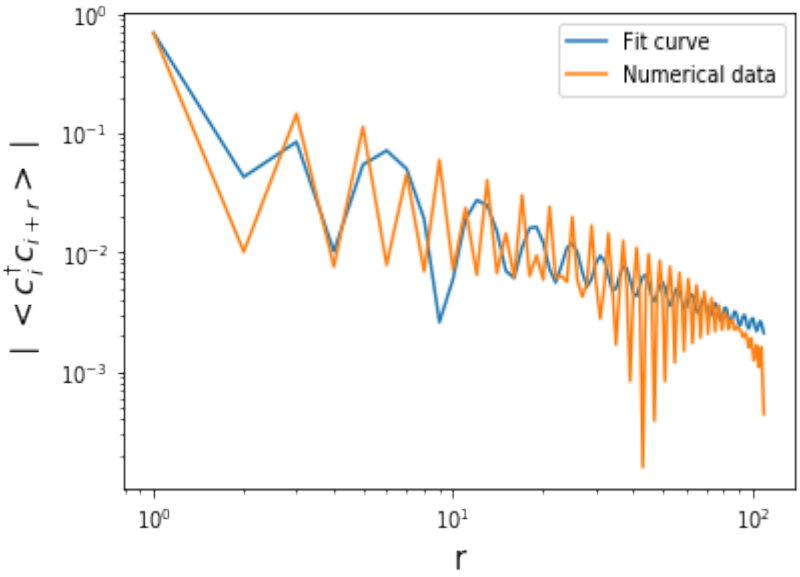

Figure 4.2: Single-particle correlator as a function of the distance for $U_1 = 4, U_2 = 2$ on a lattice of $L = 110$ sites.

where A and Δ_∞ are the fitting parameters and the latter yields the numerical estimate of the gap in the single-particle excitation spectrum in the Luttinger liquid phase. The outcome, shown in figure (4.3), seems to suggest the gapless nature of such a phase, as the extrapolated value $\Delta_\infty \approx 0.009$ turns out to be two orders of magnitude smaller than the finite-size values, contrarily to the results obtained in the gapped phases to be analyzed later.

4.2.2 Charge-density wave (•○) phase (CDW-I)

Let us now turn our attention to the strong coupling limits of the Hamiltonian (4.16) by addressing first the one we already know in more depth. If we assume that the microscopic interaction parameters take values such that the cosine term becomes relevant in the sense of the renormalization group (RG) flow, i.e. $K < K_c = \frac{1}{2}$, and that $U_1 > U_2$, so that $g < 0$, then the nature of the resulting collective behaviour becomes clear: indeed, if the RG flow for the parameter in front of the cosine interaction term drives it to strong coupling, then its effect in the framework of the low energy physics of the model consists in ordering the field around the value that minimizes the contribution of the aforesaid cosine of the field to the ground state energy of the system. The sequence of values fulfilling this condition is given by:

$$\phi_n = \frac{\pi n}{2}, \quad n \in \mathbb{Z} \tag{4.32}$$

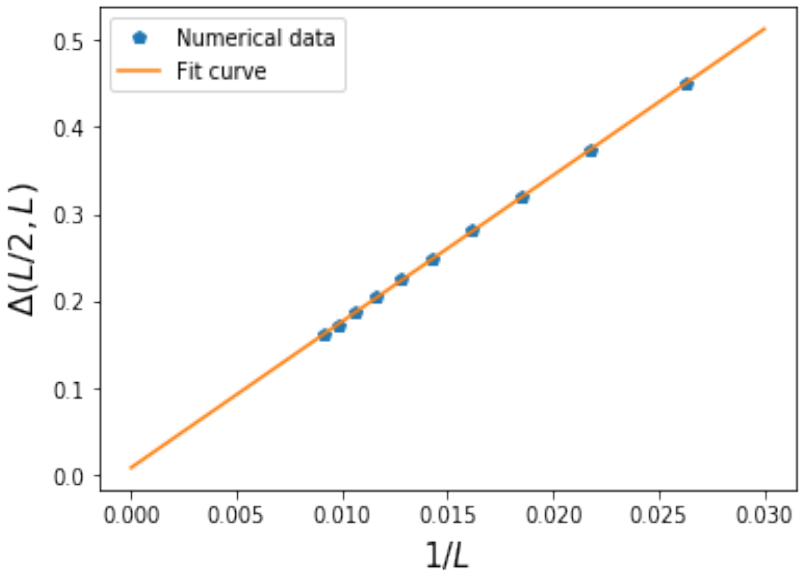

Figure 4.3: Finite-size scaling of the energy gap in the single-particle excitation spectrum for $U_1 = 4, U_2 = 2$ and lattice sizes ranging from $L = 38$ to $L = 110$ sites.

term

As a result, the computation of the properties of the phase of the model currently under analysis can be sketched in order to gain intuition with regard to its features. As a special case, let us consider once again the density profile, determined according to equation (4.22). Since the field is pinned on a constant value with arguably small fluctuations around it, the derivative term can be neglected in a first rough approximation, whereas the term $\cos[2\phi(x)]$ can be estimated as ± 1, depending on the exact value of the ordered field configuration. The final result yields:

$$\langle n_j \rangle - \frac{1}{2} \propto (-1)^{\frac{x}{a}} \tag{4.33}$$

witnessing thereby the emergence of a characteristic oscillation of the average density on the scale of the lattice constant.

Such a feature is reminiscent of the charge-ordered configuration generated by the periodic repetition of the unit cell ($\bullet\circ$), whose appearence in the phase diagram of the $t - U_1 - U_2$ model should not surprise our intuition: indeed, the Hamiltonian (4.1) reduces to the one of the XXZ model on the line $U_2 = 0$, where we know with certainty that the collective behaviour for $U_1 > 2$ is described by the aforementioned charge-ordered configuration, whch we expect to survive even at finite, sufficiently small values of U_2.

The analytical hints are reassuringly confirmed by the data produced through

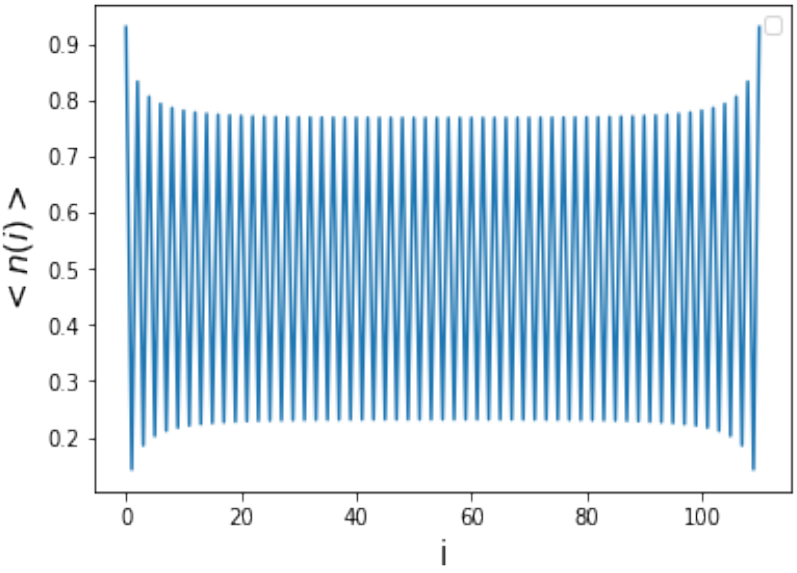

Figure 4.4: Fermionic density profile for $U_1 = 4, U_2 = 0.5$ on a lattice of $L = 111$ sites.

DMRG simulations, which confirm the existence of the CDW-I phase. Once again, the most fruitful results have been produced by characterizing the phenomenology of the system at a point predicted to belong to theCDW-I region by [2], i.e. $U_1 = 4, U_2 = 0.5$, in open boundary conditions with lattices whose dimensions vary between $L = 61$ and $L = 111$ sites. In first instance, the density profile presented in figure (4.4) shows the crystalline order characteristic of the Mott insulating state expected from the analytical treatment, for it manifestly displays a tendency towards the oscillation of the average site occupation number from an almost zero value to approximately unity when considering neighbouring sites. The deviations from the ideal picture of the crystalline phase we have depicted observed in figure (4.4) are due to the presence of non-negligible kinetic fluctuations and finite-size effects.

Simultaneously, the single-particle excitations develop a gap, which, as noted in the section devoted to the characterization of the phase diagram of the XXZ model, bosonization predicts to be related to the appearence of a mass term when studying field fluctuations around the ordered configuration. The result emerges in the outcome of the numerical simulations as well: as demonstrated in figure (4.5), the very same finite-size scaling of the aforesaid spectral property as the one performed in the Luttinger liquid phase results in an extrapolated value $\Delta_\infty \approx 0.373$ of the same order as the data points sampled at finite sizes and significantly different from zero.

In the end, consistently with emergence of massive terms in the field-theoretical

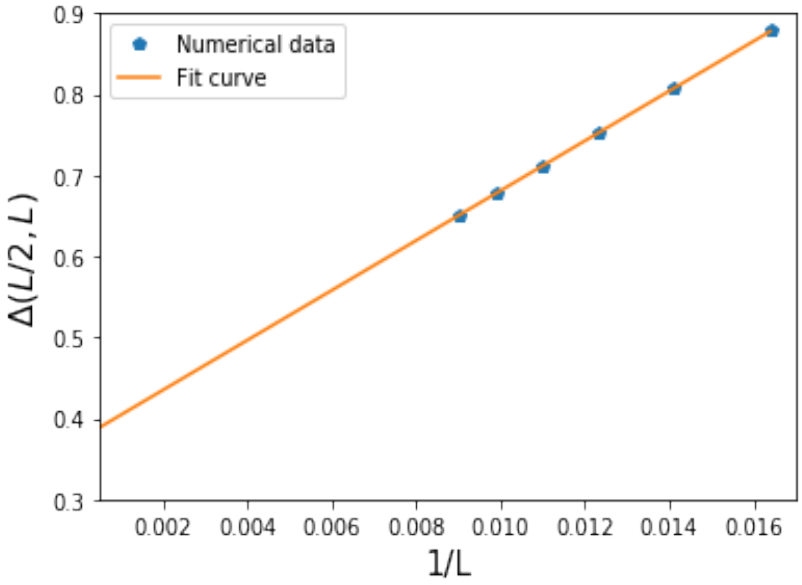

Figure 4.5: Finite-size scaling of the energy gap in the single-particle excitation spectrum for $U_1 = 4, U_2 = 0.5$ and lattice sizes ranging from $L = 61$ to $L = 111$ sites.

description of the CDW-I phase, the correlators exhibit an exponential decay over a finite length scale, called correlation length, inversely proportional to the finite gap observed in the data acquired via DMRG simulations. In order to support the above statement, figure (4.6) shows the form of the single-particle correlation function as a function of the distance, which has been fitted to a function of the form:

$$f(x; A, b, l) = A \exp\left[-\left(\frac{x}{l}\right)^b\right] \tag{4.34}$$

having denoted by A, b, l the fitting parameters. The nice agreement between the numerical data and the proposed fitting curve demonstrates the exponential trend of the single-particle correlator in the present phase, which decays over the characteristic length $l \approx 5.704$ in the case proposed in figure (4.6).

4.2.3 Bond-order (BO) phase

The last strong coupling limit of the field theory defined by (4.16) is taken into consideration by assuming not only to be in a region of the parameter space such that the cosine term is relevant, but additionally examining the case $U_2 > U_1$, which implies $g > 0$. In order to interpret the physics captured in this setting, it is worth noticing that the effect of the relevant interaction term consists again

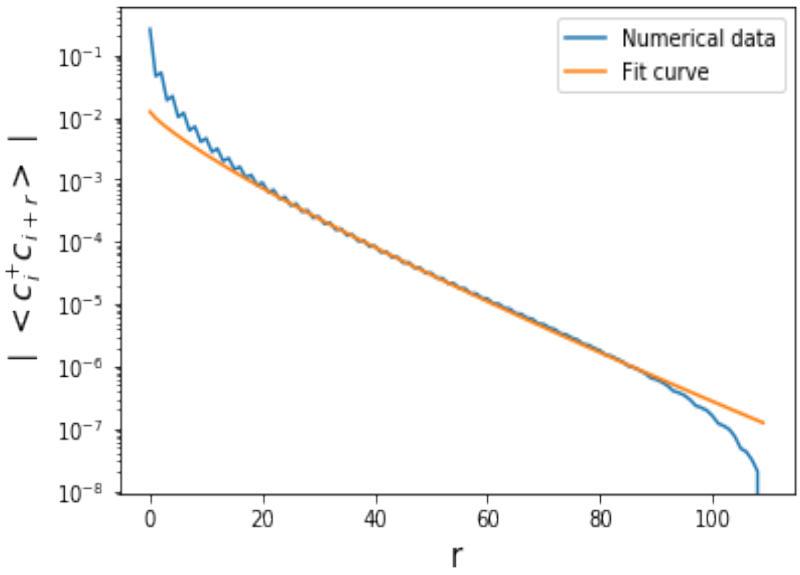

Figure 4.6: Single-particle correlator as a function of the distance for $U_1 = 4, U_2 = 0.5$ on a lattice of $L = 111$ sites.

in the realization of the pinning of the bosonic field $\phi(x)$, but the change in the sign of g with respect to the previous case results in new and unexpected properties arising from the observation that the allowed ordered configurations are now given by the sequence:

$$\phi_n = \frac{\pi}{4} + \frac{\pi n}{2}, \quad n \in \mathbb{Z} \tag{4.35}$$

Hence, following the same reasoning purposed in the previous section for the computation of the density profile, we conclude immediately that, while the derivative term in the expression of the density fluctuations in bosonization language gives roughly a zero contribution due to the ordering effect of interactions, the term $\cos[2\phi(x)]$ now vanishes as well, producing thereby the result:

$$\langle n_j \rangle \approx \frac{1}{2} \tag{4.36}$$

The above result does not differ from what has been obtained in the case of Luttinger liquids and hence arises the question on how to get the physical content of this limiting behaviour.

The answer to the aforesaid question comes from the description of the behaviour of the observable:

$$O_j = (-1)^j \left[c_j^\dagger c_{j+1} + h.c. \right] \tag{4.37}$$

in the bosonization language. The computation is readily done by plugging the expansion (4.2) into expression (4.37), expressing the fermionic field operators by means of the bosonic ones thanks to (4.11) and remembering that $e^{\pm i2k_F x}|_{x=ja} = (-1)^j$ because $k_F = \frac{\pi}{2a}$ in half-filling conditions, the final formula one arrives to can be written as:

$$O_j \propto \cos\left[2\phi(x) - \frac{\pi}{2}\right]|_{x=ja} \tag{4.38}$$

Let us take a look at the value taken by its ground state expectation value in the different phases captured by the low energy theory (4.16). On one hand, in the Luttinger liquid and CDW-I phases it can be set to zero to a first approximation. In fact, the allowed ordered configurations of the field in the CDW-I phase are chosen in such a way that $\cos\left[2\phi(x) - \frac{\pi}{2}\right]|_{\phi(x)=\phi_n} \approx 0$, where ϕ_n denotes the sequence of ordered fields for the CDW-I phase, whereas in the case of the Luttinger liquid phase it is immediate to realize that, since $\cos\left[2\phi(x) - \frac{\pi}{2}\right] = \sin\left[2\phi(x)\right]$ and the Taylor expansion of the sine function contains only products of an odd number of fields that do not contribute when averaged over a quadratic action by virtue of Wick's theorem, the ground state average of the observable O_j will result in a zero value in this case as well.

Instead, by plugging the ordered configurations of the field given by equation (4.35) in the expression for O_j, it is trivial to realize that this time the result appears to be finite. Therefore, we are now in the position to introduce the following order parameter:

$$O_{BO} = \frac{1}{L}\sum_j O_j \tag{4.39}$$

which we are going to denote as bond-order (BO) parameter. Since its expectation value is finite and different from zero only in the phase we now identify as the BO phase, it encodes the physical content of such state of matter. Indeed, as one can argue from its definition, $\langle O_{BO}\rangle$ measures the level of dimerization developed by the system, defined by the alternation of subsequent strong and weak links, where the strength of a given link is to be intended in terms of the effectiveness of the realization of hopping processes on it, quantified by means of the expectation value of the local kinetic energy operator.

Such a mysterious and counterintuitive phase can be interpreted as an energetic compromise between a Luttinger liquid and a charge-density wave ($\bullet\bullet\circ\circ$) phase, which will be characterized later. The transition from the former to the latter is not abrupt, but instead mediated by a so called BO phase, whose density profile still resembles the one of a standard Luttinger liquid, despite the fact that the system starts the process of dimerization and crystallization of the kinetic energy profile which results, upon further increasing the long-range interaction term U_2, in the establishment of the charge-ordered ($\bullet\bullet\circ\circ$) configuration.

As far as the numerical characterization is concerned, the first remarkable result is the agreement of the theoretical prediction concerning the density profile with the data extracted from the DMRG simulation carried out in open

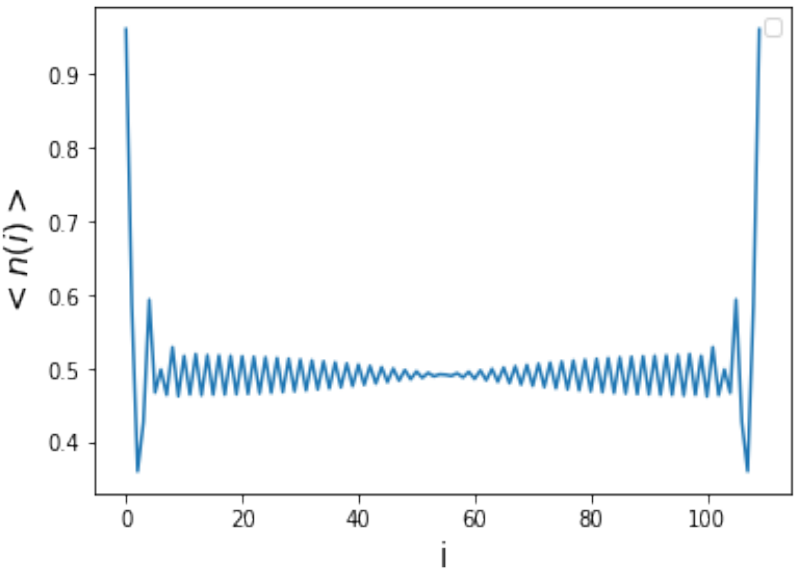

Figure 4.7: Fermionic density profile for $U_1 = 4, U_2 = 3$ on a lattice of $L = 110$ sites.

boundary conditions and with a number of lattice sites ranging from $L = 38$ to $L = 110$ at the point $U_1 = 4, U_2 = 3$, which is predicted to belong to the BO phase according to the phase diagram made available in [2]. The resulting average occupation number profile as a function of the lattice site position is proposed in figure (4.7), whose only purpose consists in making it evident that n_j does not represent the observable that allows to discriminate between the standard Luttinger liquid phase and the BO phase.

The finite-size scaling of the gap in the single-particle excitation spectrum at the aforesaid point is, on the other hand, shown in figure (4.8), whose contents need to be discussed and deeply interpreted: indeed, on one hand, since the BO phase is accompanied by the ordering of the field $\phi(x)$ in the corresponding field-theoretical characterization, one expects, in the very same way as for the case of the CDW-I phase, the emergence of mass terms responsible for the opening of a gap; on the other hand, instead, since the transition from the Luttinger liquid phase to the BO phase belongs to the Berezinskii-Kosterlitz-Thouless (BKT) universality class, the aforementioned gap Δ is known to open exponentially as a function of the distance from the transition point as:

$$\Delta \sim \exp\left(-\frac{A}{\sqrt{V - V_c}}\right) \tag{4.40}$$

where A is a constant. Hence, it is reasonable that, while extrapolating to a finite value being one order of magnitude larger than the one found in the point

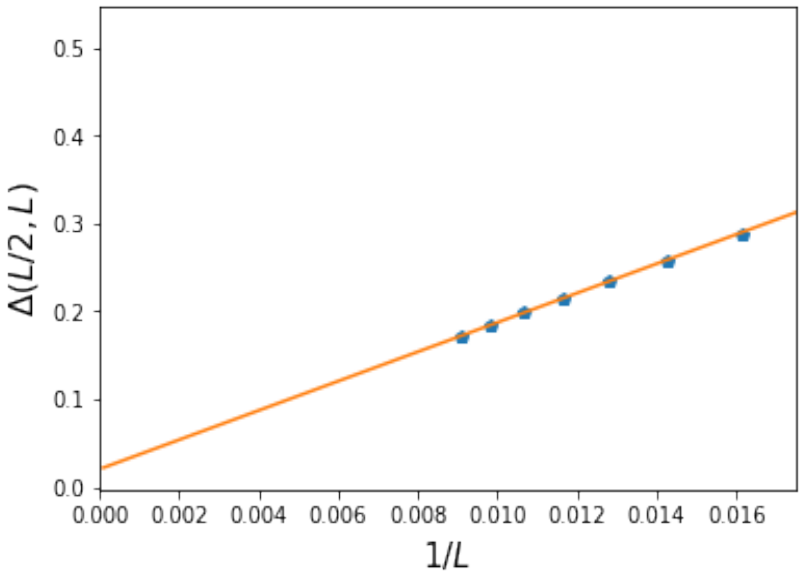

Figure 4.8: Finite-size scaling of the energy gap in the single-particle excitation spectrum for $U_1 = 4, U_2 = 3$ and lattice sizes ranging from $L = 62$ to $L = 110$ sites.

belonging to the Luttinger liquid phase, the gap in the single-particle excitation spectrum still remains small when compared to the one found in the charge-ordered configurations due to the narrow shape of the phase diagram region reserved to the mediating BO phase, which forces its interior points to lie close to the phase boundary.

As the last step of our discussion concerning the BO phase, we demonstrate in figure (4.9) the crossover from the Luttinger liquid phase to the BO phase by looking at the finite-size scaling of the BO parameter: the latter is seen to gradually extrapolate to non-zero values as the transition line proposed in the phase diagram presented in [2], thereby providing a very good agreement with their numerical data. For the sake of completeness, the results shown in figure (4.9) were obtained by performing DMRG simulations on systems with sizes varying between $L = 122$ and $L = 214$ and for parameter values satisfying $U_1 = 4, 2.3 \leq U_2 \leq 2.7$, whereas the fitting procedure has been carried out with the functional form:

$$f(L; O_{BO,\infty}, B) = O_{BO,\infty} + \frac{B}{\sqrt{L}} \tag{4.41}$$

where $O_{BO,\infty}$ and B are fitting parameters and the $x^{-\frac{1}{2}}$ decay has been chosen, following [20] and [21], by assuming that O_{BO} scales as L^{-K}, L being the system size, in the Luttinger liquid phase and knowing that $K = \frac{1}{2}$ at the transition

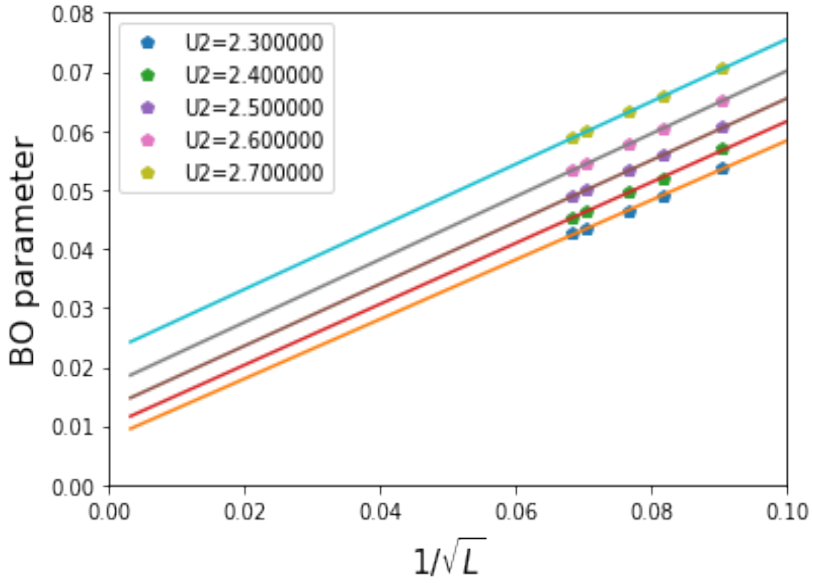

Figure 4.9: Finite-size scaling of the BO parameter for $U_1 = 4, 2.3 \leq U_2 \leq 2.7$ and lattice sizes ranging from $L = 122$ to $L = 214$ sites.

line.

4.2.4 Charge-density wave (••○○) phase (CDW-II)

The last form of collective behaviour exhibited by the system is the charge-ordered phase resulting from the periodic repetition in space of the unit cell (••○○). Such a configuration is not captured by our weak-coupling bosonization approach, which does not reproduce the aforesaid density profile and only accounts for the dimerization process leading to the CDW-II when the interaction term U_2 reaches non-perturbative finite values. Hence, the data presented for the CDW-II will be exclusively numerical.

The data have been obtained by characterizing the nature of the phenomenology of the system at the point $U_1 = 4, U_2 = 6$ through DMRG simulations on lattices whose size varies between $L = 38$ and $L = 110$ sites. The density profile, provided in figure (4.10), exhibits manifestly the periodic, Mott insulating configuration described above, apart from the standard slight deviations from the ideal behaviour due to the finite kinetic fluctuations and the enhancement of the average occupation number at the edges of the system, which does not fulfill the requirement of translational invariance as a result of the adopted open boundary conditions. Additionally, the numerical simulations show with outstanding evidence in figure (4.11) the opening of a gap in the single-particle excitation spectrum, consistently with the expectation of a

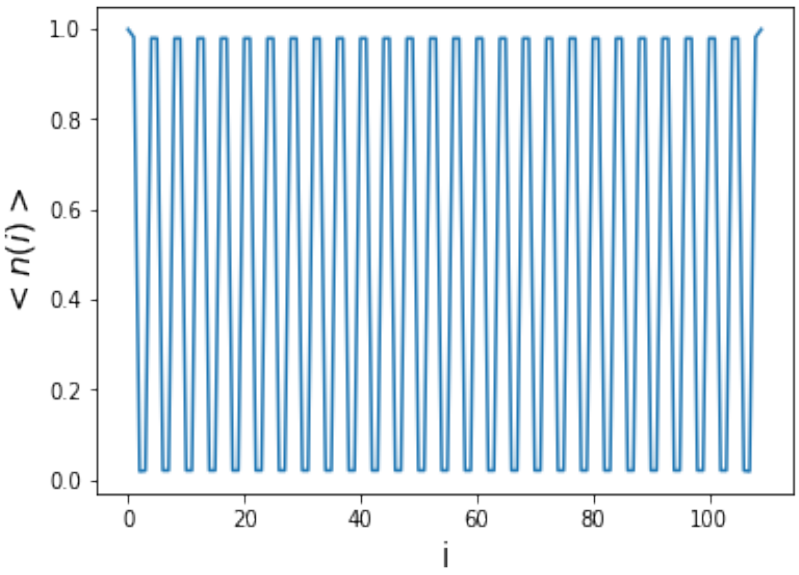

Figure 4.10: Fermionic density profile for $U_1 = 4, U_2 = 6$ on a lattice of $L = 110$ sites.

finite gap in a charge-ordered, Mott insulating state. The analysis proceeds, as usual, through an extrapolation to the thermodynamic limit of the values obtained in the finite-size sample, where the fitting procedure has been performed via the expression (4.31), providing thereby an estimate $\Delta_\infty \approx 8.237$. In perfect analogy with the behaviour emerged in the characterization of the CDW-I phase, the long-range, discrete translational symmetry breaking order characterizing the CDW-II phase is therefore equipped with short-range correlations, as witnessed by the exponential decay of the single-particle correlation function over a finite correlation length, as figure (4.12) shows explicitly by fitting the numerical data to the exponentially decaying curve:

$$f(x; A, l, \omega) = Ae^{-\frac{x}{l}} \cos(\omega x) \tag{4.42}$$

having indicated the fitting parameters as A, l, ω.

As a last remark, it is worth investigating the finite-size scaling of the BO parameter as a function of the system size in the CDW-II phase: as expected on the ground of our physical intuition, the dimerization process is taken to its extreme consequences by increasing U_2 while fixing the other model parameters to a constant value. The local kinetic energy profile exhibits an alternation from finite to almost zero values over a 1 lattice constant step, as one can argue from figure (4.13). Such a behaviour results quite obviously in a finite, comparatively large value of the BO parameter, whose extrapolation to the thermodynamic limit confirms the dimerized nature of the CDW-II phase, as shown in figure

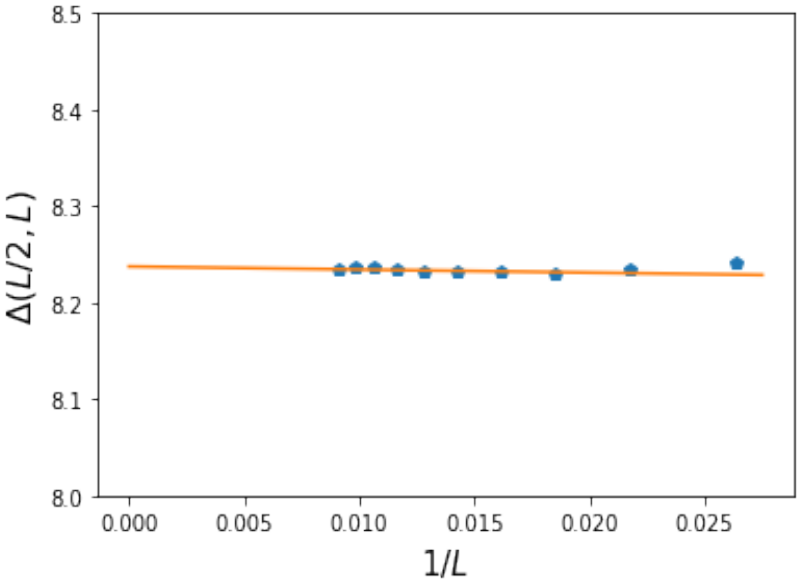

Figure 4.11: Finite-size scaling of the energy gap in the single-particle excitation spectrum for $U_1 = 4, U_2 = 0.5$ and lattice sizes ranging from $L = 61$ to $L = 111$ sites.

(4.14). The fitting curve, which shows an almost perfect agreement with the experimental data, has been chosen on purely phenomenological grounds to take the form of a decaying power law, i.e.:

$$f(L; O_{BO,\infty}, B, m) = O_{BO,\infty} + \frac{B}{L^m} \tag{4.43}$$

where $O_{BO,\infty}, B, m$ are the fitting parameters and $O_{BO,\infty}$ is our estimate for the infinite-size value of O_{BO}. In the present case, it takes the value $O_{BO} \approx 0.129$, which turns out to be of the same order of magnitude of the sampled data points and confirms the presence of long.range order associated to the BO parameter in the CDW-II phase.

4.2.5 Central charge

The concluding part of the work on the half-filled $t-U_1-U_2$ model concerns the search for signatures of the occurence of phase transitions between the various phases discussed above by means of the central charge profile. Roughly speaking, the latter quantity is defined in the framework of conformal field theory, where it enters the definition of the Virasoro algebra attached to a given field theory. Without entering the discussion of further details which go beyond the scope of the present work, the central charge can be related to the entanglement properties of the system via the celebrated Cardy-Calabrese formula (see

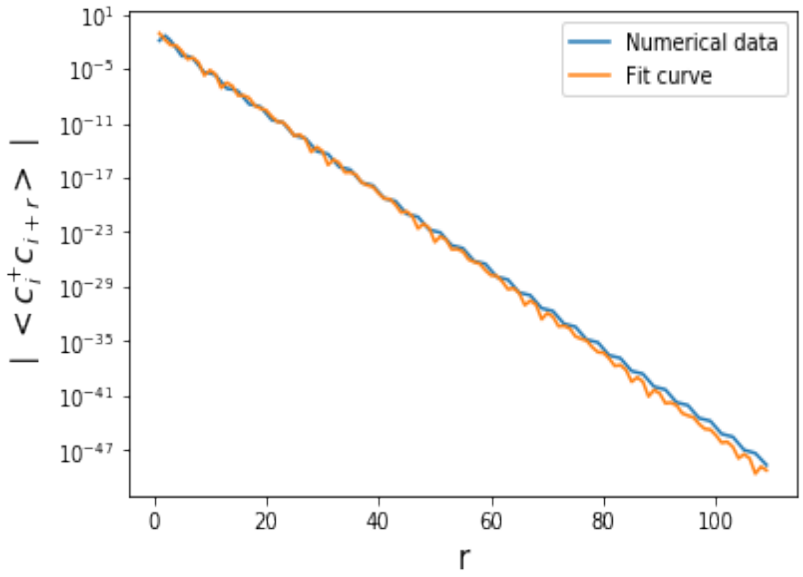

Figure 4.12: Single-particle correlator as a function of the distance for $U_1 = 4, U_2 = 6$ on a lattice of $L = 110$ sites.

[22]), which provides us with the scaling relation fulfilled by the bipartite von Neumann entanglement entropy of a conformal field theory as:

$$S_A = -Tr\left(\rho_A \log \rho_A\right) \tag{4.44}$$

where ρ_A refers to the density matrix of the subsystem A with respect to the rest of the chain. The aforesaid Cardy-Calabrese relation reads:

$$S(l) \approx \frac{c}{6} \log \left[\frac{L+1}{\pi} \sin\left(\frac{\pi x}{L+1} \right) \right] + a_0 \tag{4.45}$$

where we have indicated the length of the whole system as L, the length of the subsystem as l, the central charge as c and a_0 represents a constant. Additional finite-size corrections to (4.45) have not been reported.

As far as the numerical characterization is concerned, the DMRG simulations were performed along the line $U_1 = 4$, while varying U_2 between the values $U_2 = 0$ and $U_2 = 6$ and keeping the system size fixed to $L = 61$ lattice sites in the phase diagram region interested by the CDW-I phase and to $L = 62$ lattice sites when analyzing the CDW-II phase. The apparently bizarre change in the number of lattice sites keeps track of the commensurability condition the lattice has to satisfy in order to accomodate the corresponding charge-ordered phase without introducing frustrated configurations. The central charge has been extracted from the numerically obtained entanglement entropy profile by fitting

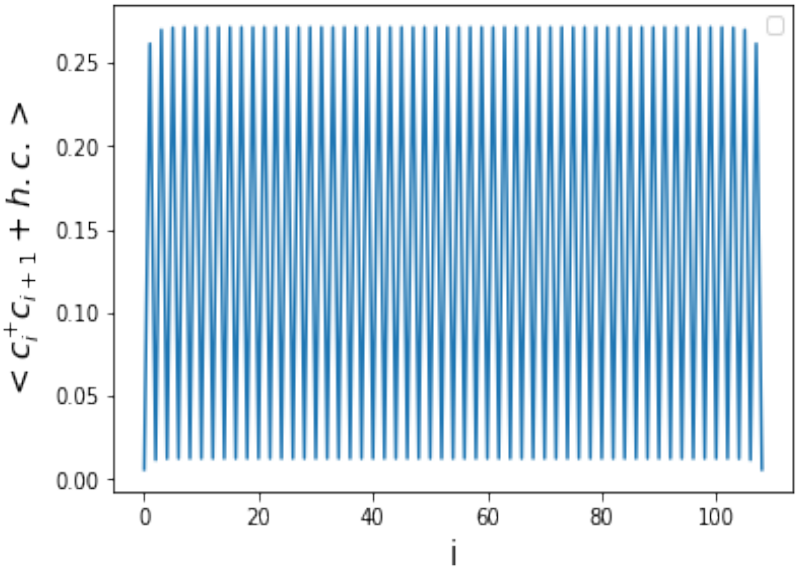

Figure 4.13: Local kinetic energy profile for $U_1 = 4, U_2 = 6$ on a lattice of $L = 110$ sites.

it to equation (4.45), thereby treating the central charge c and the constant a_0 as fitting parameters.

The result one obtains is shown in figure (4.15). The findings exhibit a significantly good agreement with the phase diagram proposed in [2]. indeed, starting from $U_2 = 0$, where the system's behaviour is the one in the CDW-I phase, the central charge assumes at first values which are very close to zero; then, upon further increasing the value of U_2, the central charge starts increasing until it reaches values close to unity in correspondence of the transition, approximately located around $U_2 = 1.2$ by such a treatment, from the CDW-I phase to the Luttinger liquid phase, which is known to be described by a conformal field theory with central charge $c = 1$. Subsequently, around the value $U_2 = 2.5$, a downward jump of the value of the central charge signals that the system is entering the BO phase, whereas, when including even larger values of U_2, a cusp in the central charge profile around $U_2 = 4$ followed by the subsequent decay of the central charge to almost zero value signals the transition to the charge-ordered CDW-II phase. The numerical values of the transition points along the analyzed cut in the phase diagram turn out to be a posteriori close to the more finely determined ones proposed in [2].

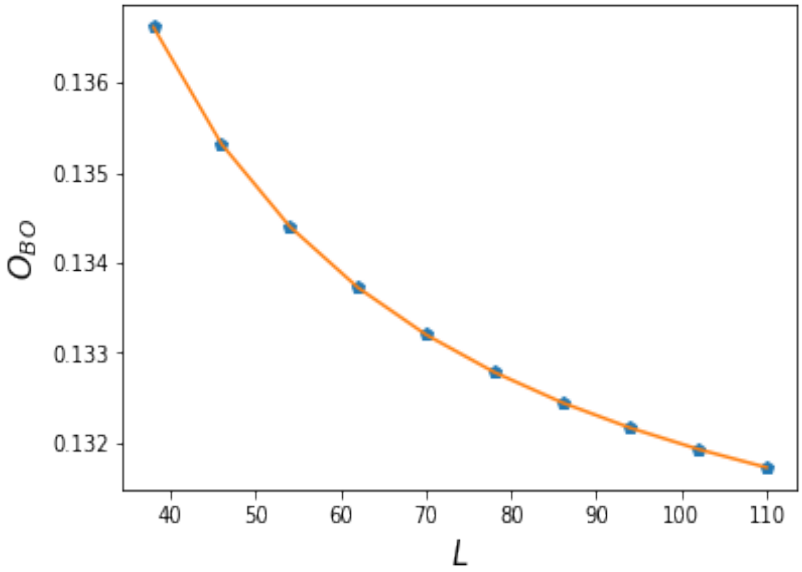

Figure 4.14: Finite-size scaling of the BO parameter for $U_1 = 4, U_2 = 6$ and lattice sizes ranging from $L = 38$ to $L = 110$ sites.

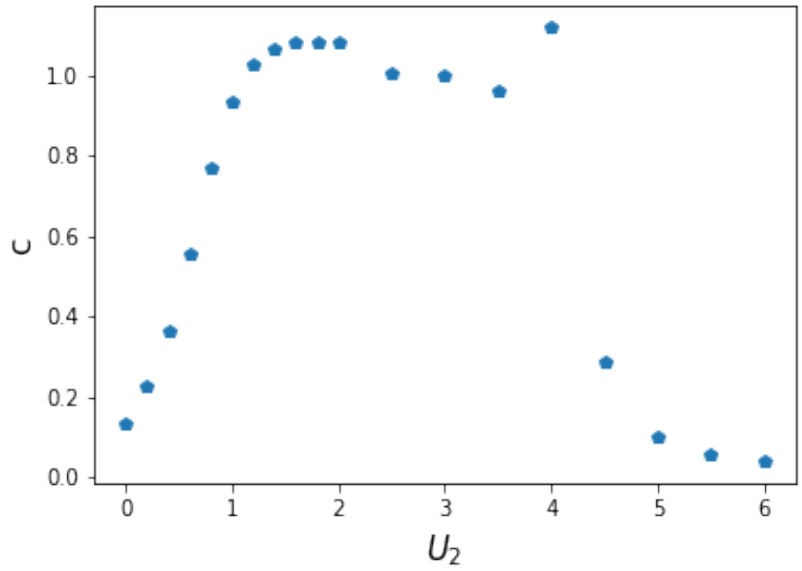

Figure 4.15: Central charge profile along the cut $U_1 = 4, 0 \leq U_2 \leq 6$ on lattices of $L = 61$ and $L = 62$ sites.

Chapter 5

$t - U_1 - U_2$ model at $n = 0.4$ filling

5.1 Introduction

The general aim of the present chapter is the discussion of the first numerical results obtained by moving away from the half-filling condition in the framework of the $t-U_1-U_2$ model. The characterization of the behaviour of the system at the density $n = 0.4$ that will be given in the following pages is still far from being systematic and only represents a starting point for a future deeper analysis of such a theoretical setup.

As mentioned in the introduction to the present thesis work, the scientific literature has already started to deal with analogous problems. We remind, e.g., the argument presented in [5], where M. Dalmonte et al. showed, in the case of bosonic hard-core particles, that the $t-U_1-U_2$ model exhibits a transition from a standard Luttinger liquid phase to a cluster Luttinger liquid phase along the line $U_1 = U_2 = U > 0$, where only repulsive interactions have been considered.

The long-term purpose of our decision of pursuing research activity in this direction can be found in the pioneering idea brought about in [3] and [18], where a first discussion of the topological physics aspects arising from the presence of interfaces between weak and strong pairing liquid regions is presented. We will therefore search for the aforementioned phases in the framework of the $t - U_1 - U_2$ model by moving away from the half-filling condition with the clue that the CDW-II phase will turn into a strong pairing liquid phase upon decreasing the density, so that it will be possible to move on to the treatment of theoretical models exhibiting signatures of topological physics such as Majorana zero-energy modes.

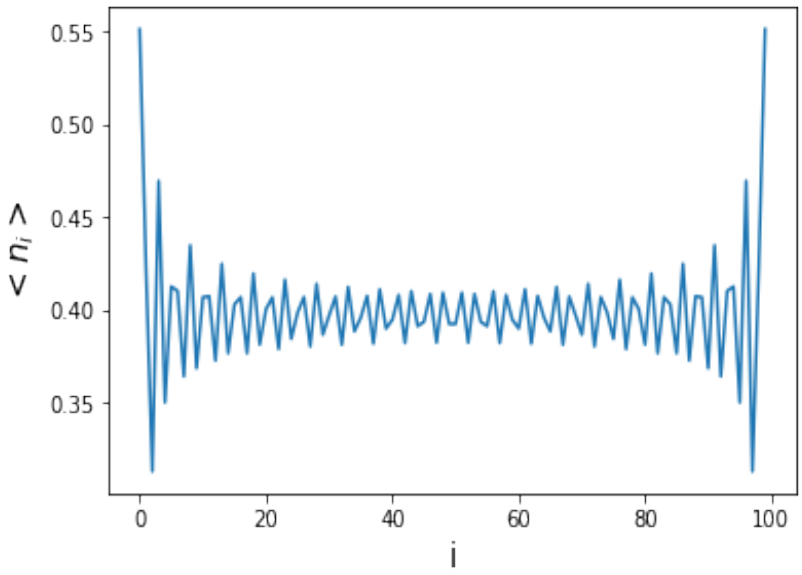

Figure 5.1: Fermionic density profile exhibited by the system for $U_1 = U_2 = 1$ on a lattice of $L = 100$ sites.

5.2 Numerical results

Let us now draw our attention to the description of the phenomenology observed until now in the $n = 0.4$ fermionic $t - U_1 - U_2$ model. In first instance, the analysis has been carried out by observing how the density profile of the system changes along the lines $U_1 = U_2$ and $U_1 = \frac{U_2}{2}$ for positive interaction parameter values, while the lattice size has been fixed to the value $L = 100$, enforcing therefore the number of fermions to be $N = 40$.

For sufficiently small values of the interaction strengths, the system seems is adiabatically connected to the non-interacting point $U_1 = U_2 = 0$, thereby exhibiting the characteristic behaviour of a Luttinger liquid. Among its signatures, we report here both the density profile and the single-particle quasi-long-range-order.

The former exhibits the behaviour shown in figure (5.1), i.e. small oscillations around the uniform configurations and a typical enhancement of the average occupation number at the edges; both features are once again perfectly reasonable in view of the fact that all DMRG simulations have been carried out in open boundary conditions, thereby breaking translational invariance while being far from the infinite-size limit.

The latter is instead demonstrated in figure (5.2) by the profile of the single-particle correlator as a function of the distance, which has been fitted to a power

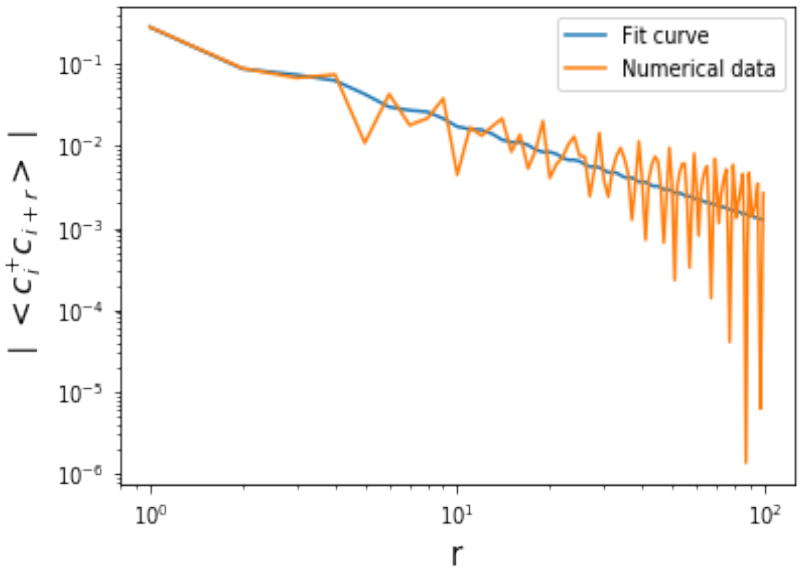

Figure 5.2: Single-particle correlator as a function of the distance for $U_1 = U_2 = 1$ on a lattice of $L = 100$ sites.

law of the form:

$$f(x; A, b, C, \omega, e) = \frac{A}{x^b} + C\frac{\cos(\omega x)}{x^e} \tag{5.1}$$

where A, b, C, ω, e are to be interpreted as fitting parameters.

The actual novelty with respect to the half-filled case arises when one tries to increase further the value of the interaction parameters: as the central charge profile extracted from the fit of the bipartite von Neumann entanglement entropy as a function of the values of U_1 and U_2 and shown in figure (5.3) suggests, the weakly-interacting regime is confirmed to behave as a standard Luttinger liquid phase, since values of the central charge c close to unity agree with the analytical finding that the Luttinger liquid Hamiltonian can be thought of as a $c = 1$ theory in the framework of CFT. On the other side, around the value $U_c^{(1)} \approx 5$ in the case of the cut along the $U_1 = U_2 = U$ line and $U_c^{(2)} \approx 4$ with regard to the line $U_2 = 2U_1 = U$, the entanglement entropy stops following the behaviour predicted by the Cardy-Calabrese formula, thereby signaling a transition to a different state of matter which is worth further investigation, and the resulting values for the central charge obtained by means of a fit to the aforesaid Cardy-Calabrese law become nonsensical.

Armed with the purpose of gaining some intuition with regard to the collective behaviour emerging above the aforementioned roughly determined critical values of the interaction strength, the density profile of the system deep in the strong-coupling regime is presented in figure (5.4) along the line $U_1 = U_2$ (the

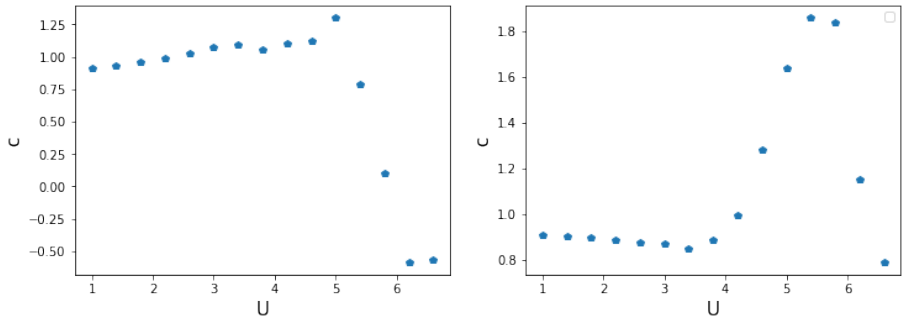

Figure 5.3: On the left: central charge profile for $U_1 = U_2 = U$ varying between $U = 1$ and $U = 6.6$ on a lattice of $L = 100$ sites. On the right: central charge profile for $U_2 = 2U_1 = U$ varying between $U = 1$ and $U = 6.6$ on a lattice of $L = 100$ sites.

results in the other case turn out to be completely analogous). The system develops a form of phase separation: by such an expression we mean that the open boundary conditions enforce a local optimal configuration at the boundaries with the shape of a highly irregular crystal which extends over a finite, presumably non-extensive distance from the edges; the profile in the bulk, instead, can be approximately described as the periodic repetition of the unit cell $(\bullet \circ \circ)$, which can be trivially recognised as one of the charge-ordered configurations whose structure is such that the contribution of the interaction energy terms proportional to U_1 resp. U_2 to the ground state energy gets completely suppressed. Of course, it cannot be extended over the whole system, since it would require the filling to be $n = \frac{1}{3}$, contrarily to the present case $n = \frac{2}{5} > \frac{1}{3}$.

It is to be noticed that the above decribed configuration arises further questions concerning the convergence of the DMRG variational optimization procedure, since it could eventually differ from the strict ground state of the system and represent instead one of the possibly many metastable states of the DMRG procedure characterized by pseudocrystalline arrangement and near-degeneracy in the energy spectrum between each other and with respect to the true ground state as well. The latter feature may make it hard to escape from the multitude of metastable configurations and reach the global energy minimum of the system by means of a local optimization procedure on the wavefunction.

The described picture of the energy landscape and the multitude of energetically metastable configurations finds its foundations in the behaviour of the model in the classical limit $t = 0$ (see [5]), which is expected to be approximated in the large interaction strength limit, i.e $\frac{U}{t} \ll 1$: the system exhibits an exponentially large (in the system size) number of degenerate ground state configurations realized by successions of N_A blocks of the form $(\bullet \bullet \circ\circ)$ and N_B blocks of the type $(\bullet \circ \circ)$, where the ratio $\frac{N_A}{N_B}$ takes the value $\frac{1}{2}$ for a density $n = \frac{2}{5}$. Interestingly, the density profile shown in (5.4) is not extremely far from

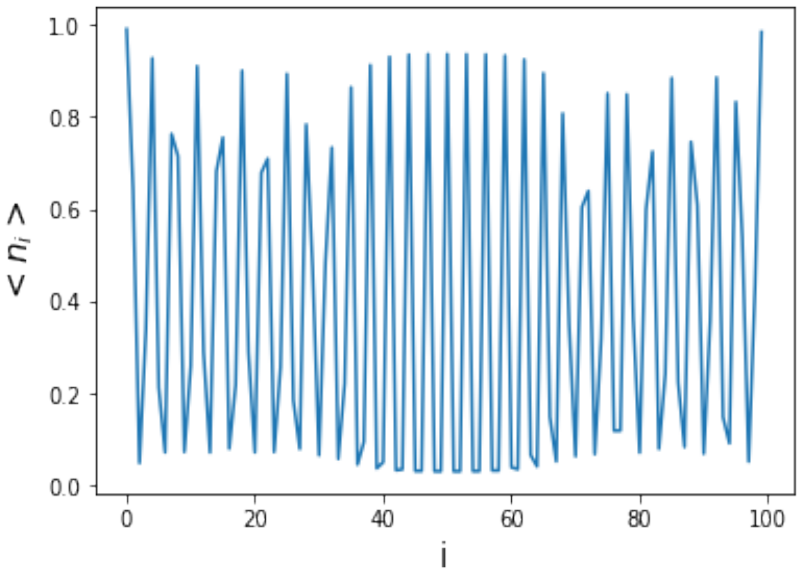

Figure 5.4: Fermionic density profile exhibited by the system for $U_1 = U_2 = 6.6$ on a lattice of $L = 100$ sites.

the picture of the system in the classical limit, even if plagued by finite-size effects and presumably affected by the convergence issues of the DMRG algorithm in presence of kinetic fluctuations, which turn the exact degeneracy of the classical grond states into a near-degeneracy condition which may be identified as one of the most prominent reason for the metastability-related numerical difficulties.

As a concluding, fascinating remark, let us look at the spectral properties of the system at the transition point between the two aforesaid collective behaviours along the cut $U_1 = U_2$. The simulations have been inspired by the analysis performed in [5] on the quantities:

$$\Delta(N, L) = E(N-1, L) + E(N+1, L) - 2E(N, L) \tag{5.2}$$

$$\Delta_{cl}(N, L) = E(N-2, L) + E(N+2, L) - 2E(N, L) \tag{5.3}$$

where, as usual, $E(N, L)$ indicates the ground state energy of the system with N particles on a lattice of L sites. While $\Delta(N, L)$ represents the energy gap in the single-particle excitation spectrum, $\Delta_{cl}(N, L)$ is defined in [5] as the cluster gap and is intended to probe the nature of the low energy excitations of cluster degrees of freedom across the transition point.

As demonstrated in figures (5.5) and (5.6), when considering the behaviour of the quantities defined in equations (5.2) and (5.3) while varying $U_1 = U_2 = U$ across the critical value $U_c^1 \approx 5.605$ (as accurately estimated in [5]), it emerges that such a transition can be characterized by the opening of a finite non-zero

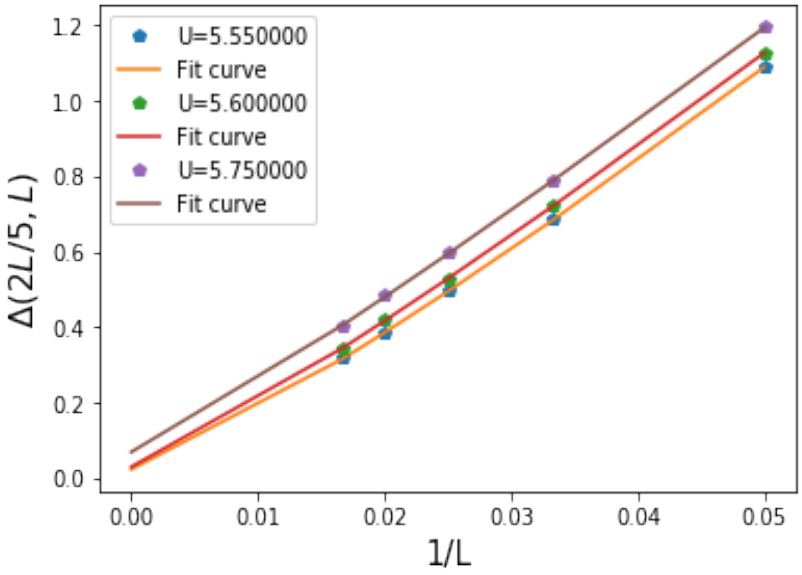

Figure 5.5: Finite-size scaling of the energy gap in the single-particle excitation spectrum for the values of $U_1 = U_2 = U$ reported in the figure on lattices with sizes ranging between $L = 20$ and $L = 60$.

energy gap in the single-particle excitation spectrum, while, on the other hand, the cluster gap continues to extrapolate to an almost zero value in a way that looks independent from the precise value of the interaction strength U close to the phase boundary.

The data have been fitted to the power law functional form:

$$f(x; \Delta_\infty, A, m) = \Delta_\infty + \frac{A}{x^m} \tag{5.4}$$

where Δ_∞, A, m are the fitting parameters and Δ_∞ has been taken as the estimate of the corresponding gap in the infinite-size limit. On one hand, the cluster gap values are seen to lose at least one order of magnitude when extrapolated to the thermodynamic limit, reaching thereby values of order $10^{-2} - 10^{-3}$ which, given the inclusion of finite-size effects and the limited number of data points, can be safely assumed to demonstrate the absence of a cluster gap. On the other hand, the single-particle gap starts to open, as captured by its infinite-size values, which moves upwards from values $\Delta_\infty \approx 0.02 - 0.03$ up to $\Delta_\infty \approx 0.07$ and is expected to increase further with the interaction strength U.

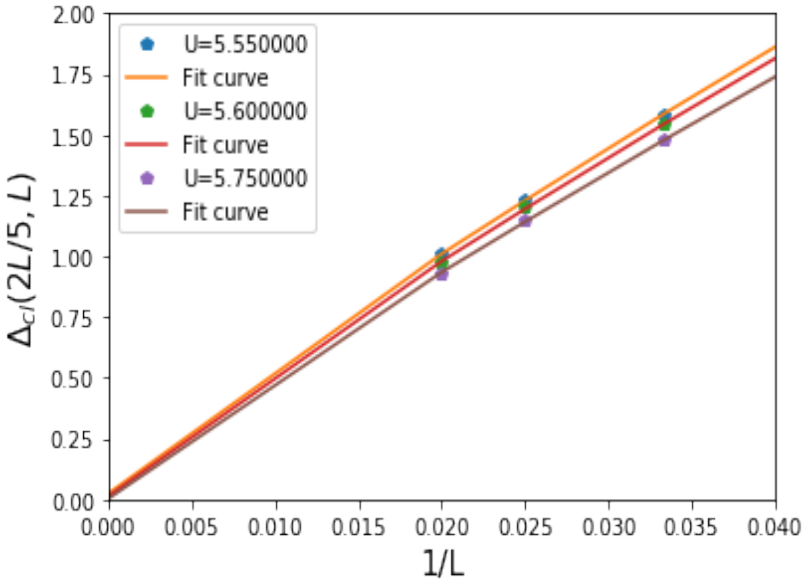

Figure 5.6: Finite-size scaling of the cluster gap for the values of $U_1 = U_2 = U$ reported in the figure on lattices with sizes ranging between $L = 30$ and $L = 50$.

Chapter 6

Conclusions

The present thesis work has been written with the main goal of tackling the phenomenology resulting from the presence of long-range interactions in the framework of strongly-correlated low-dimensional quantum systems. After a quick review of the literature on the aforesaid topic, one immediately realizes that the latter is not a merely speculative research field reserved to theorists only, but instead raises the interest of the experimental groups working on cold-atoms setups in effectively one-dimensional (1D) regimes, where long-range interactions may be introduced by employing Rydberg atoms for quantum simulation purposes.

Then, armed with the purpose of investigating the phase diagram of a many-fermion lattice model, the report has moved on to the review of the state-of-the art techniques for the study of 1D many-body quantum physics which have been used in the remainder of the text. In particular, the numerical tool employed for the characterization of the different phases of the model under investigation by means of the computation of order parameters and correlation functions is represented by the celebrated DMRG algorithm, whose working principle consists in an optimal truncation of the full, exponentially large Hilbert space of the many-body problem to a proper subspace of it, in such a way that the low energy properties of the model remain largely unaffected by the approximation.

Simultaneously, the field-theoretical approach to the 1D many-body problem has been introduced by proposing a derivation of the bosonization prescription. The latter allows to formulate effective bosonic field theories describing the low energy physics of,e.g., lattice models. In particular, once the bosonic representation of the system is known, the standard route to get both qualitative and quantitative informations concerning the physics of the one-dimensional system under analysis relies on the application of standard field-theoretical techniques, such as path integral calculations and renormalization group (RG) analysis, to the derivation of the large distance behaviour of the correlation functions and the characterization of the critical properties of the system.

Then, both original DMRG simulations and bosonization calculations have been performed with the goal of understanding the properties of the collec-

tive behaviour displayed by the well known XXZ model. In more detail, the transition from the Luttinger liquid phase to the antiferromagnetic long-range ordering has been described by presenting a RG argument with reference to the effective low energy theory formulated by means of the bosonization technique and obtaining the functional forms of the various correlators in each of the two phases, while presenting numerical evidence for the analytical findings through the data analysis carried out on the outcomes of the DMRG simulations.

The focus of the thesis work has then been the recharacterization of the phase diagram of the $t - U_1 - U_2$ model at half-filling, whose derivation from a purely numerical point of view has already been proposed in [2]. Besides crosschecking the accuracy of the phase diagram reported in [2], we achieved in the formulation of a low energy effective theory which captures the main qualitative features of the phase diagram of the model and gives a very great deal of insight into the nature of the competing ordering mechanisms originating from the simultaneous presence of the interaction parameters U_1 and U_2.

While being able to recover the transition already encountered in the study of the XXZ model in the limit where the interaction strength U_2 is negligible when compared to U_1, the opposite scenario shows instead that the ordering mechanism induced by the next-to-nearest-neighbour interaction realizes a tendency towards dimerization across the whole system, so that consecutive bonds between contiguous lattice sites display a finite difference in the average local kinetic energy content, while the uniform density profile typical of the Luttinger liquid phase is still mantained. Such a scenario is complemented, in the limit of even larger U_2, by the numerical evidence of a charge-density wave configuration with unit cell $(\bullet\bullet\circ\circ)$, which is to be intuitively interpreted as the phase resulting from the long-range bond-order when driving the system towards the non-perturbative regime of large values of the interaction strength U_2.

Finally, the purpose of the concluding chapter of the thesis report consists mainly in the presentation of the perspectives of the future research efforts we envision on the path towards a more complete understanding of the role of long-range interactions in the framework of the topological properties of one-dimensional systems. Concretely, the results of the first DMRG simulations on the $t - U_1 - U_2$ model at filling $n = 0.4$ have been presented, thereby pointing out the most interesting observations we have been able to formulate and at the same time enlightening the possibly severe computational difficulties emerging at first sight.

Bibliography

[1] Giamarchi, T., 2004, *Quantum Physics in One Dimension* (Oxford University Press, Oxford).

[2] T. Mishra et al., Phys. Rev. B 84, 115135 (2011).

[3] J. Ruhman et al., Phys. Rev. B 96, 085133 (2017).

[4] M Szyniszewski et al., Phys. Rev. B 98 (7), 075139 (2018).

[5] M. Dalmonte et al., Phys. Rev. B 92, 045106 (2015).

[6] U. Schollwck, Reviews of Modern Physis 77, 259 (2005).

[7] U. Schollwck, Annals of Physics, 326, 96 (2011).

[8] T. L. Nguyen et al., Phys. Rev. X 8, 011032 (2018).

[9] D. Barredo et al., Science 354, 1021 (2016).

[10] V. Lienhard et al., *Observing the space- and time-dependent growth of correlations in dynamically tuned synthetic Ising antiferromagnets*, arXiv:1711.01185 (2017).

[11] H. Bernien et al., *Probing Many-Body Dynamics on a 51-Atom Quantum Simulator*, Nature (London) 551, 579 (2017).

[12] E. Miranda, Braz. J. Phys. 33, 3 (2003).

[13] S Eggert, A pedestrian approach to bosonization, arXiv:cond-mat/0807.0003v2 (2007).

[14] J. von Delft and H. Schoeller, Bosonization for Beginners Refermionization for Experts, Ann. Phys. (Leipzig) 7 (1998) 225.

[15] R. Shankar, Acta Phys. Pol. B 26, 1835 (1995).

[16] F. D. M. Haldane, J. Phys. C 14, 2585 (1981).

[17] ITensor, http://itensor.org.

[18] J. Ruhman, E. Berg, and E. Altman, Phys. Rev. Lett. 114, 100401 (2015).

[19] A. Y. Kitaev, Physics-Uspekhi 44, 131 (2001).

[20] S. Ejima and S. Nishimoto, Phys. Rev. Lett. 99, 216403 (2007).

[21] S. R. White , I. Affleck, and D. J. Scalapino , Phys. Rev. B 65, 165122 (2002).

[22] P. Calabrese and J. Cardy, Journal of Physics A: Mathematical and Theoretical 42, 504005 (2009).

[23] S. Sachdev, Quantum Phase Transitions (Cambridge University Press, Cambridge, 2002).

[24] N. Goldenfeld, *Lectures on Phase Transitions and Renormalization Group* (Addision Wesley, 1992)

[25] Bruus, H., and K. Flensberg, *Many-Body Quantum Theory in Condensed Matter Physics: An Introduction* (Oxford University Press, Oxford,2004).

[26] Schau, P. et al., *Observation of spatially ordered struc- tures in a two-dimensional Rydberg gas*, Nature 491, 87- 91 (2012).

[27] N. Nagaosa, *Quantum Field Theory in Strongly Correlated Electronic Systems*, (Springer Science and Business Media, 1999).

[28] A. Keesling et al., Nature 568, 207 (2019).

[29] R. P. Feynman, International Journal of Theoretical Physics 21 (1982), 467.

[30] S. Lloyd, Science 273 (1996), 1073.

[31] M. Saffman, T. Walker, and K. Mlmer, Rev. Mod. Phys. 82, 2313 (2010).

[32] M. V. Rakov, M. Weyrauch, and B. Braiorr-Orrs, *Sym- metries and entanglement in the one-dimensional spin-$\frac{1}{2}$ XXZ model*, Phys. Rev. B 93, 054417 (2016).

[33] S. R. White, Phys. Rev. Lett. 69, 2863 (1992).

[34] S. R. White, Phys. Rev. B 48, 10345 (1993).

Appendix A

The density matrix renormalization group

A.1 Historical remarks and general considerations

The goal of the present section is a quick review of the key conceptual ideas which represent the theoretical foundations of the celebrated density matrix renormalization group (DMRG) algorithm. The latter represents the state-of-the-art technique in the numerical characterization of the low energy properties of one-dimensional (1D) systems. The purpose of this section does not consist in giving an extensive review of the topic, but instead a quick introduction. Further details can be found in the reviews by Schoellwock ([6], [6]).

It is well known that the main obstacle to the efficiency of the numerical simulations of quantum many-body systems is the exponentially increasing size of the Hilbert space as a function of the system size. As an example, a standard spin-$\frac{1}{2}$ model defined on a lattice of size L is endowed with a Hilbert space $\mathcal{H}$ given by the tensor product of the local spin-$\frac{1}{2}$ Hilbert spaces. The corresponding basis is written formally as:

$$\mathcal{B}_{\mathcal{H}} = \left\{ |\sigma\rangle_1 \otimes |\sigma\rangle_2 \otimes \cdots \otimes |\sigma\rangle_L : \sigma = \pm\frac{1}{2} \right\} \tag{A.1}$$

where L is the number of lattice sites. A trivial computation reveals that the dimension of the aforementioned Hilbert space $\mathcal{H}$ equals 2^L, thereby proving the point made above with regard to the Hilbert space dimension. Hence, the exact diagonalization routines turn out to suffer from unavoidable restrictions in the limit of large systems, even though they have reached high levels of sophistication and in certain circumstances represent the only way to tackle a given physical problem.

In order to circumvent such a fundamental limitation which is intrinsic to the nature of the many-body problem, the approach adopted by the DMRG

procedure is variational in its essence, for it amounts to the computation of the low energy properties of the system by performing computational steps and optimization procedures in a proper subspace of the full exponentially large Hilbert space.

Since its invention in 1992 by Steve White (see [33] and [34]), the DMRG algorithm has become the most popular numerical technique in the study of strongly correlated low-dimensional quantum systems. While initially its use was limited to the study of static properties of the low-lying eigenstates of the Hamiltonian of interest such as energy, order parameters and n-point correlation functions, afterwards the method was extended to the computation of dynamical and finite-temperature properties of the model.

A.2 The algorithm

In order to deal with the exponential growth of the Hilbert space dimension, the core of the DMRG algorithm relies on the implementation of an efficient truncation scheme of the Hilbert space by means of a local decimation procedure. The crucial conceptual foundation of the current reasoning is the assumption that the low energy properties of the system are captured by a numerically manageable reduced state space identified by means of a rigorous criterion.

The first step of the DMRG procedure is traditionally denoted as infinite-system DMRG and proceeds iteratively by growing a long chain through the addition of pairs of local degrees of freedom at each step. Formally, let us consider two sublattices (blocks in the DMRG language) of size l, denoted respectively as A and B, whose Hilbert spaces $\mathcal{H}_A$ and $\mathcal{H}_B$ are in principle equipped with the bases $\mathcal{B}_A = \{|i\rangle_A : 1 \leq i \leq dim(\mathcal{H}_A)\}$ resp. $\mathcal{B}_B = \{|j\rangle_B : 1 \leq i \leq dim(\mathcal{H}_B)\}$. For efficiency purposes, let us suppose additionally that our numerical resources allow us to deal with a truncated state space of dimension D for the two aforesaid blocks with basis $\mathcal{B}'_A = \{|\alpha\rangle_A : 1 \leq \alpha \leq D\}$ resp. $\mathcal{B}'_B = \{|\beta\rangle_B : 1 \leq \beta \leq D\}$, so that we can at most achieve an effective description of the sublattices A and B in a proper subspace of the full Hilbert space. Then, by enlarging the lattice through the addition of two sites in the middle, the questions one should try to answer to concern the determination of the ground state of the superblock $A \bullet \bullet B$ of length $2l + 2$ and the derivation of a reduced basis of dimension D for the blocks $A\bullet$ and $\bullet B$.

As a first remark, any state $|\psi\rangle$ defined on the superblock $A \bullet \bullet B$ can be expanded in the reduced basis of the Hilbert space of the superblock as:

$$|\psi\rangle = \sum_{i=1}^{D} \sum_{m=1}^{d} \sum_{n=1}^{d} \sum_{j=1}^{D} c_{imnj} |\alpha\rangle_A |m\rangle_{l+1} |n\rangle_{l+2} |\beta\rangle_B \tag{A.2}$$

where $|m\rangle_{l+1}$ and $|n\rangle_{l+2}$ denote the basis elements of the Hilbert space attached to the local degree of freedom. Hence, the ground state of the superblock, i.e.

the state ψ minimizing the quantity:

$$E[\psi] = \frac{\langle\psi|H_{A\bullet\bullet B}|\psi\rangle}{\langle\psi|\psi\rangle} \tag{A.3}$$

is found by numerical diagonalization of the Hamiltonian, whose matrix representation has dimension $d^2D^2 \times d^2D^2$, where d is the dimension of the local Hilbert space. The numerical recipies typically employed to achieve such a goal are iterative sparse matrix eigensolvers such as the ones provided by the Lanczos and Jacobi-Davidson methods.

After having answered the first question, let us turn our attention to the determination of a truncated basis of the Hilbert space of the enlarged block $A\bullet$ and similarly of $\bullet B$ by means of a sensible criterion. Naively, if one takes the set of states $\{|\alpha\rangle_A|m\rangle_{l+1}\}$ as the new basis for the Hilbert space of $A\bullet$, it is immediate to realize that its dimension has grown to dD, yielding thereby exponential growth as a function of the number of iterations of the algorithmic procedure. Hence, a cutoff procedure needs to be implemented in order to avoid exponential growth.

By defining:

$$\rho_{A\bullet} = Tr_{\bullet B}(|\psi\rangle\langle\psi|) \tag{A.4}$$

$$\rho_{\bullet B} = Tr_{A\bullet}(|\psi\rangle\langle\psi|) \tag{A.5}$$

it is possible to state that the choice of the algorithm consists in retaining the D eigenvectors of the reduced density matrix $\rho_{A\bullet}$ with largest eigenvalues as an effective basis for the new block $A\bullet$. The same reasoning applies of course for the block $\bullet B$ with regard to the reduced density matrix $\rho_{\bullet B}$. The number D is usually referred to as number of kept states or bond dimension in the scientific literature. The justification for the aforesaid procedure can be understood by considering the following optimization problem: since the wavefunction of a quantum system encodes the whole amount of information about it, we may be tempted to find the optimal wavefunction $|\tilde{\psi}\rangle$ in a subspace of given dimension D that minimizes the L^2-norm distance $|||\psi\rangle - |\tilde{\psi}\rangle||_2$ from the actual ground state wavefunction $|\psi\rangle$.

The problem is equivalent to the well known low-rank approximation of a matrix: indeed, interpreting the coefficients of the expansion of the ground state wavefunction with respect to an orthonormal basis, the above problem reduces to the determination of the matrix $\tilde{\Psi}$ of rank D that best approximates the ground state matrix Ψ formed by the aforementioned coefficients with respect to the Frobenius norm $||\cdot||_F$, defined by the relation:

$$||M||_F = \sum_{i,j} |M_{ij}|^2 \tag{A.6}$$

where M is a generic matrix.

By applying the well known singular value decomposition (SVD) to the $dD \times dD$ matrix Ψ, it can be rewritten in the form:

$$\Psi = U\Sigma V^\dagger \tag{A.7}$$

where U and V are unitary matrices, Σ is a diagonal matrix with real non-negative entries called singular values and all matrices have dimension $dD \times dD$ in our specific setting. Then, the optimal choice of $\tilde{\Psi}$ is given by:

$$\tilde{\Psi} = U\Sigma' V^\dagger \tag{A.8}$$

where Σ' is obtained from Σ by setting to zero all but the D largest singular values.

Switching to the bra-ket notation, it means that, while the actual ground state of the system can be expressed as:

$$|\psi\rangle = \sum_{a=1}^{dD} s_a |a\rangle_{A\bullet} |a\rangle_{\bullet B} \tag{A.9}$$

its approximation reads:

$$|\psi\rangle = \sum_{a=1}^{D} s_a |a\rangle_{A\bullet} |a\rangle_{\bullet B} \tag{A.10}$$

having denoted the singular values as s_a and assumed them to be sorted in decreasing order ($s_1 \geq s_2 \geq \cdots \geq s_{dD}$) and defined:

$$|a\rangle_{A\bullet} = \sum_{i=1}^{dD} U_{ia} |i\rangle_{A\bullet} \tag{A.11}$$

$$|a\rangle_{\bullet B} = \sum_{j=1}^{dD} V^*_{ja} |j\rangle_{\bullet B} \tag{A.12}$$

where $|i\rangle_{A\bullet}$ and $|j\rangle_{\bullet B}$ represent the dD basis elements of the blocks $A\bullet$ and $\bullet B$, respectively.

Finally, in order to make connection with the above reference to the reduced density matrices of the bipartite system, it is sufficient to realize that, since the states $|a\rangle_{A\bullet}$ and $|a\rangle_{\bullet B}$ are defined through the application of a unitary transformation to the elements of a complete set of orthonormal states, they represent themselves a valid basis choice. Therefore, the trace operation defining the reduced density matrices of the two blocks is easily carried out and gives the following as a result:

$$\rho_{A\bullet} = \sum_{a=1}^{dD} s_a^2 |a\rangle_{A\bullet} \langle a|_{A\bullet} \tag{A.13}$$

$$\rho_{\bullet B} = \sum_{a=1}^{dD} s_a^2 |a\rangle_{\bullet B} \langle a|_{\bullet B} \tag{A.14}$$

Equations (A.13) and(A.14) clarify that the states defined in (A.11) and(A.12) are the eigenvectors of $\rho_{A\bullet}$ resp. $\rho_{\bullet B}$, while the spectrum of the two operators

coincides. Thus, the approximation made in (A.10) truly amounts to neglecting the eigenvectors of the reduced density matrices associated to their smallest eigenvalues.

After having performed the steps detailed above, the algorithm repeats them in presence of two additional sites added in the middle of the system. Then, once the desired system size is reached as a result of the application of the infinite-system DMRG procedure, it is crucial to follow up on it by the so called finite-system DMRG procedure. Roughly speaking, the finite-system DMRG algorithm improves the choice of the reduced basis for superblocks being much smaller than the desired system size.

Concretely, the algorithm works almost identically to the infinite-system one: at each step, the ground state of the superblock is computed, the eigensystem of the reduced density matrices are found and the D eigenvectors with largest eigenvalues are retained for the characterization of the successive superblock. The only difference with respect to the above procedure lies in the fact that the growth of one of the two blocks by one site occurs at the expense of the other. This continues until the shrinking block's Hilbert space reaches a dimension which does not exceed D and is followed by the reversal of the growth direction. The described sweeping procedure, when repeated until the wavefunction converges, has been shown to radically change in most of the cases the results given by the sole application of the infinite-system DMRG algorithm, so that its implementation in the currently used DMRG codes is undeniable.

A.3 DMRG and matrix-product-states

As a last remark, it is worth remarking a different formulation of the whole DMRG procedure entirely based on the matrix-product-state (MPS) representation of a quantum many-body state. The latter, in first instance, allows for an exact description of a generic quantum state of a, e.g., lattice model $|\psi\rangle = \sum_{\{s_i\}} c_{s_1 \dots s_N} |s_1\rangle \dots |s_N\rangle$ by reexpressing it as:

$$|\psi\rangle = \sum_{\{s_i\}} \sum_{\{\alpha_i\}} A^{[s_1]}_{\alpha_2} A^{[s_2]}_{\alpha_2 \alpha_3} \dots A^{[s_{L-1}]}_{\alpha_{L-1} \alpha_L} A^{[s_L]}_{\alpha_L} |s_1\rangle \dots |s_N\rangle \tag{A.15}$$

The issue with the expression in (A.15) is the exponentially increasing dimension of the A matrices when one tries to perform exact calculations. However, it turns out that the formula presented in (A.15) yields an efficient parametrization of the subspace the DMRG algorithm works on when the dimension of the aforesaid matrices is reduced to a given cutoff value D, which coincides with the bond dimension of the iterative update procedure. The unprecedented flexibility and simplicity characterizing the art of manipulating MPS has made the formulation and implementation of the DMRG code in the MPS formalism the choice of preference in the scientific community.